

Summer 7-15-2019

# Post-Polymerization Modification of Kapton Using Electron Beam Irradiation

Luis A. Hernandez  
*University of New Mexico*

Follow this and additional works at: [https://digitalrepository.unm.edu/me\\_etds](https://digitalrepository.unm.edu/me_etds)



Part of the [Mechanical Engineering Commons](#)

---

## Recommended Citation

Hernandez, Luis A.. "Post-Polymerization Modification of Kapton Using Electron Beam Irradiation." (2019).  
[https://digitalrepository.unm.edu/me\\_etds/169](https://digitalrepository.unm.edu/me_etds/169)

This Thesis is brought to you for free and open access by the Engineering ETDs at UNM Digital Repository. It has been accepted for inclusion in Mechanical Engineering ETDs by an authorized administrator of UNM Digital Repository. For more information, please contact [amywinter@unm.edu](mailto:amywinter@unm.edu).

Luis A. Hernandez

---

*Candidate*

Mechanical Engineering

---

*Department*

This thesis is approved, and it is acceptable in quality and form for publication:

*Approved by the Thesis Committee:*

Mehran Tehrani , Chairperson

---

Sakineh Chabi

---

Daniel Engelhart

---

**POST-POLYMERIZATION  
MODIFICATION OF KAPTON  
USING ELECTRON BEAM IRRADIATION**

by

**Luis A. Hernandez**

**B.S., Mechanical Engineering  
University of New Mexico, 2018**

THESIS

Submitted in Partial Fulfillment of the  
Requirements for the Degree of

**Master of Science  
Mechanical Engineering**

The University of New Mexico  
Albuquerque, New Mexico

**July 2019**

## ACKNOWLEDGEMENTS

I would first like to thank the experts who were involved in the experimentation of this Masters' Thesis research: Scientists Dr. Daniel Engelhart, and Mr. Ryan Hoffman. Their office was always open when I required guidance and had a question about the research or writing. Dr. Engelhart met with me a few times on weekends to answer many of the questions I had and create list of objectives to meet next. I am truly grateful for the passion, involvement, and input received from him.

I would also like to thank my thesis advisor and professor Dr. Mehran Tehrani from the University of New Mexico. In the absence of time, he assisted with my Masters' thesis and timeline objectives ensuring proper protocol was met. Additionally, he provided invaluable feedback during every presentation update given during our meetings. His valuable recommendations have shaped my educational and professional development.

Finally, I must express my very profound gratitude to my fiancé, Angellia, for providing me with an enormous amount of encouragement and support throughout both my undergrad and graduate studies. In addition, the process of researching and writing this thesis was amongst the most difficult obstacles in my educational career. This accomplishment would not have been possible without her.

**POST-POLYMERIZATION  
MODIFICATION OF KAPTON  
USING ELECTRON BEAM IRRADIATION**

**by**

**Luis A. Hernandez**

**B.S. Mechanical Engineering, University of New Mexico  
M.S. Mechanical Engineering, University of New Mexico**

**ABSTRACT**

In the present study, the feasibility of chemical modification of electron-irradiated Kapton is investigated. Characterization techniques determined the changes between a pristine, electron irradiated, and a chemically treated, i.e., fluorinated, sample of Kapton. Kapton is a common material in space application as it serves as the exterior surface for space vehicles. Highly aged Kapton have significant material property changes, making them prone to electrostatic discharge (ESD) damage. Understanding how Kapton material behaves under space conditions and the possibility of improving its structure and properties is of utmost important. To this end, changes to the physical properties of the material were probed using volume conductivity measurements, Fourier Transform Infrared (FTIR) absorption spectroscopy, and mechanical testing. The research suggests that although the electron irradiation or fluorination can be employed to tailor the chemical structure and optical properties of Kapton, it is not highly efficient in altering its mechanical and electrical properties.

# Table of Contents

<b>ABSTRACT</b> .....	<b>iv</b>
<b>List of Tables</b> .....	<b>ix</b>
<b>List of Abbreviations</b> .....	<b>x</b>
<b>List of Symbols</b> .....	<b>xi</b>
<b>Chapter 1: Background</b> .....	<b>1</b>
1.1 Electron Aging and Space Weather .....	2
1.2 Healing after Electron Irradiation.....	6
1.3 Motivation .....	7
1.4 Literature Review .....	8
1.4.1 Brush-type Surface Modification .....	9
1.4.2 Electrical Aging in Polyimide .....	10
1.4.3 Improved Adhesion Techniques.....	11
1.4.4 Boron Bearing Kapton.....	12
1.4.5 Gas Evolution During Electron irradiation.....	13
1.4.6 Specificity of Ion Induced Damage .....	15
1.4.7 ReaxFF Simulations .....	15
<b>Chapter 2: Experimental Procedures</b> .....	<b>19</b>
2.1 Jumbo Vacuum Chamber .....	22
2.2 Electrical Conductivity .....	24
2.3 Spectroscopy .....	31
2.4 Tensile Testing .....	40
<b>Chapter 3: Results and Discussion</b> .....	<b>44</b>
3.1 Electrical Conductivity Results.....	46
3.2 FTIR Spectroscopy Results .....	51
3.2 Tensile Properties.....	57
<b>Chapter 4: Conclusions and Future Work</b> .....	<b>61</b>
<b>References</b> .....	<b>63</b>

## Table of Figures

Figure 1: Proton flux model for circular Earth orbits <sup>5</sup> .....	3
Figure 2: Electron flux model for circular Earth orbits <sup>5</sup> .....	3
Figure 3: Energy deposited in 76 $\mu\text{m}$ thick Kapton by 90 keV electron beam <sup>15</sup> .....	6
Figure 4: SPD curves of PI samples measured before and after exposure of irradiated PI to partial pressures of (a) argon, (b) nitrogen, (c) oxygen, and (d) water vapor. <sup>11</sup> .....	7
Figure 5: Chloromethylation and azide decoration process <sup>21</sup> .....	9
Figure 6: FTIR spectra of pristine and aged 100HN PI at room temperature <sup>22</sup> .....	10
Figure 7: Peel strength as a function of weight increased taken up by graft polymerization <sup>23</sup> .....	12
Figure 8: Electrical conductivity of PI and PI-SB films measured at room temperature <sup>24</sup> .....	13
Figure 9: Experimental setup of irradiated samples <sup>25</sup> .....	14
Figure 10: Yield of evolved gases vs. dose for Kapton after electron beam irradiation: (O) total gas, ( $\Delta$ ) $\text{H}_2$ , ( $\square$ ) $\text{CH}_4$ (x 10), ( $\bullet$ ) $\text{CO}$ , ( $\bullet$ ) $\text{CO}_2$ , and ( $\blacktriangle$ ) $\text{N}_2$ (x 100) <sup>25</sup> .....	14
Figure 11: Simulated Kapton slab and positions of “electron beams.” See text for further discussion. <sup>28</sup> .....	16
Figure 12: Snapshots of the expansion of the polyimide in the X and Y directions in separate simulations <sup>28</sup> .....	17
Figure 13: Strain-stress graph of the polyimide slab before and after electron beam exposures as calculated using ReaxFF force field calculations. <sup>28</sup> .....	18
Figure 14: Binder vacuum chamber .....	19
Figure 15: Pfeiffer vacuum pump .....	20
Figure 16: Kapton sample mounted on the carousel .....	20
Figure 17: Jumbo Environmental Simulation Chamber <sup>29</sup> .....	22
Figure 18: Electron beam flux at 90 keV with rastering as a function of time <sup>29</sup> .....	24
Figure 19: A Single Conductor <sup>31</sup> .....	24
Figure 20: A Double Conductor <sup>31</sup> .....	25
Figure 21: Representative charge/discharge curve of PI material bombarded with non-penetrating electrons. Shaded areas represent the three regions of the charge/discharge curve. <sup>32</sup> .....	27
Figure 22: Electrical conductivity measurement test setup .....	28

Figure 23: 3"x 3" pristine Kapton sample on the test fixture .....	29
Figure 24: Current as a function of time performed at 250V for the pristine sample.....	30
Figure 25: Current as a function of time performed at 250V for the pristine sample; statistical error bars .....	31
Figure 26: Newton studying the refraction of light <sup>35</sup> .....	32
Figure 27: Energy, Wavelength, and Molecular Effects <sup>37</sup> .....	33
Figure 28: Stretching and bending vibrations in molecules <sup>38</sup> .....	34
Figure 29: FTIR spectrum of Hexane <sup>39</sup> .....	35
Figure 30: Benzene and Phenyl group molecular structures <sup>40</sup> .....	35
Figure 31: Kapton chemical structure: poly-oxydiphenylene-pyromellitimide <sup>42</sup> .....	36
Figure 32: FTIR design schematic .....	37
Figure 33: The Nicolet 6700 experimental setup (Left); Sampling plate (Right).....	38
Figure 34: Tensile stress and cross-sectional area <sup>46</sup> .....	40
Figure 35: Tensile strain diagram <sup>46</sup> .....	41
Figure 36: Stress & Strain diagram <sup>47</sup> .....	42
Figure 37: Tension clamp experimental setup <sup>48</sup> .....	42
Figure 38: Non-homogenous electron aged sample. Time of post-irradiation atmospheric exposure is indicated below each panel. ....	44
Figure 39: Electron aged sample healing process. Time of post-irradiation atmospheric exposure is indicated below each panel. ....	45
Figure 40: Fluorinated sample healing process. Time of post-irradiation atmospheric exposure is indicated below each panel. ....	46
Figure 41: Electrical conductivity error bars .....	49
Figure 42: FTIR spectra of pristine, electron aged, and fluorinated samples .....	51
Figure 43: Normalization at the phenyl absorption peak .....	52
Figure 44: Normalized FTIR spectra of pristine, electron aged, and fluorinated samples .....	53
Figure 45: Close-up of the CO <sub>2</sub> doublet peak .....	54
Figure 46: FTIR spectrum of CO <sub>2</sub> <sup>50</sup> .....	55
Figure 47: FTIR spectra of all experimental samples in addition to two highly electron irradiated PI films .....	56
Figure 48: Stress versus strain graph of the Pristine sample .....	58

Figure 49: Representative stress - strain graphs .....59

## List of Tables

Table 1: Electron gun settings and Faraday cup readings.....	20
Table 2: Vibrational assignments of polyimide <sup>44-45</sup> .....	39
Table 3: Pristine sample; First experimental electrical conductivity measurements .....	46
Table 4: Aged sample; First experimental electrical conductivity measurements .....	47
Table 5: Fluorinated sample; First experimental electrical conductivity measurements.....	47
Table 6: Pristine sample; Second experimental electrical conductivity measurements .....	48
Table 7: Aged sample; Second experimental electrical conductivity measurements .....	48
Table 8: Fluorinated sample; Second experimental electrical conductivity measurements ...	49
Table 9: Mechanical properties of pristine, aged, and fluorinated Kapton.....	57

## List of Abbreviations

ESD	Electro-Static Discharge
FTIR	Fourier Transform Infrared
DMA	Dynamic Mechanical Analysis
ASTM	American Society for Testing and Materials
ZPD	Zero Path Difference
OPD	Optical Path Difference
PMMA	Poly(methyl methacrylate)
PS	Polystyrene
PI	Polyimide
DMF	Dimethylformamide
MCT	Mercury cadmium telluride
PEEK	Poly(aryl ether ether ketone)
PES	Poly(aryl ether sulphone)
U-PS	Udel poly(aryl sulphone)
U-Polymer	Poly(aryl ester)
DMA	Dynamic Mechanical Analysis
MEO	Medium Earth Orbit
GEO	Geosynchronous Earth Orbit
NIST	National Institute Standards and Technology
SPD	Surface Potential Decay
SDOM	Standard Deviation of the Mean
SEM	Scanning Electron Microscopy
XPS	X-ray Photoelectron Spectroscopy
XRD	X-ray Diffraction

## List of Symbols

$\propto$	proportional
A	cross-sectional area
F	force
g	distance between the guarded electrode and the ring electrode
I	Current
K	Kelvin
$K_v$	effective area of the guarded electrode for the particular electrode arrangement deployed
L	original length of specimen
$L_w$	width of the sample
N	Newton
Pa	Pascal
R	resistance
t	average thickness of the sample
$t_c$	average thickness of the sample in centimeters
u	relative length of deformation
v	lateral deformation
V	Voltage
$\beta$	effective area coefficient
$\varepsilon$	tensile strain
$\varepsilon_L$	lateral strain
$\rho$	Resistivity
$\rho_v$	Volume Resistivity
$\sigma$	tensile stress
$\sigma_c$	Conductivity
$\Omega$	ohms
$D\emptyset$	effective diameter of the guarded electrode

## Chapter 1: Background

Technological advancements have evolved with the help of materials science over the last century. Kapton is a polyimide (PI) used for various applications, including aircraft, electronics, and medical devices. Kapton is used because of its high mechanical strength, insulating properties, low density, flexibility, and resistance to space radiation. In the space industry, Kapton mainly serves as the exterior surface of a satellite, offering an ultra-lightweight thermal and electrical insulator to provide a stable range of operating temperatures for satellite systems, as well as shielding electronic componentry from the space environment through which the spacecraft travels in. Kapton is also known to be chemically stable over a wide range of temperature fluctuations.

The space environment is filled with hazards to spacecraft and instrumentation. Some of these include high energy charged particles, intense thermal cycles, atomic oxygen, and orbital debris. One of the most detrimental effects of space weather on satellites is the Electro-Static Discharge (ESD). High electric fields arise due to the interactions between the spacecraft and the ambient space environment. A discharge occurs when an electric field gradient exists across a material in excess of that material's dielectric breakdown potential. ESD can have catastrophic consequences for the mission, such as structural damage, degradation of spacecraft subsystems, and operational difficulties caused by damages to electronics.

The bombardment of spacecraft by energetic particles induce several destructive and non-destructive changes in constituent satellite materials. Non-destructive processes can result in electronic and vibrational excitation, electron emission, radiation-induced conductivity, and a host of other effects that can alter spacecraft material behavior over a wide range of time scales.<sup>1-3</sup> The destructive processes lead to chemical changes in spacecraft materials with a subsequent change of the material's physical properties or aging. Highly aged samples are susceptible to ESD effects, destructive to the spacecraft materials, that must be investigated.

During the irradiation of Kapton with high energy electrons, its chemical structure is changed, resulting in the formation of new, highly reactive, chemical states. This offers an advantageous approach for tailoring properties of Kapton. As such, exposure of the irradiated material to a chosen chemical reactant will allow manipulation of Kapton properties. In the presented work, the Kapton sample was mounted in a vacuum chamber and bombarded with

fully penetrating electrons, followed by flooding the chamber with a chemical reactant. Any change to the Kapton would take place before an equilibrium state is reached or before it heals. Exposing the irradiated polymer to a fluence of the appropriate reactant should lead to chemical modification due to radicals reacting to form chemical bonds with the reactant. That modification will lead to changes in the chemical, conductive, and mechanical properties of the enhanced material compared to the aged and pristine samples.

The volume conductivity measurements indicated no change in bulk conductivity that was greater than experimental error. FTIR measurements showed significant differences between pristine, electron aged, and fluorinated Kapton samples. In addition to small changes across the spectra between pristine and treated Kapton samples, a new doublet peak emerged in the absorption spectra of the electron aged and fluorinated samples, corresponding to carbon dioxide (CO<sub>2</sub>) formation. The emergence of this double peak is attributed to the evolution of CO<sub>2</sub> gas from the material as a result of chemical damage during electron irradiation. This effect was more pronounced for the fluorinated samples. Tensile testing indicated increased Young's modulus after electron irradiation, indirectly indicating crosslinking and chain scission.

## 1.1 Electron Aging and Space Weather

Depending on the space environment, it may be inevitable for a material to be exposed to a large dose of energized particles. The natural Geosynchronous Earth Orbit (GEO) environment comprises electrons and protons with a broad spectrum of particle energies as well as solar ultraviolet (UV) radiation. Other particles are present in GEO, including gamma rays, but in terms of total energy deposition into a spacecraft, solar charged particles and UV photons are the dominant species interacting with the spacecraft surface.

The scientific community uses statistical models such as the AP9 and AE9 to represent mean flux values for protons and electrons under circular Earth orbits, as shown in **Figure 1** and **Figure 2** below.<sup>4</sup> The mean flux values were acquired by a satellite in circular geocentric orbit as a function of altitude and maximum latitude. The dashed lines are representative of typical orbits including positions of the International Space Station (ISS), the moon, and other major satellites.

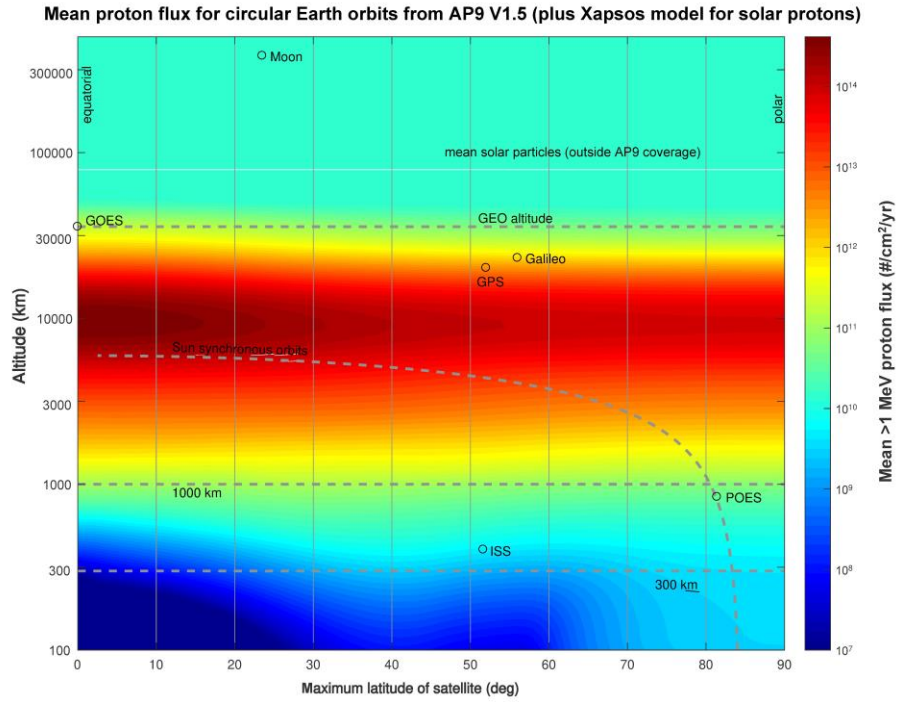


Figure 1: Proton flux model for circular Earth orbits<sup>5</sup>

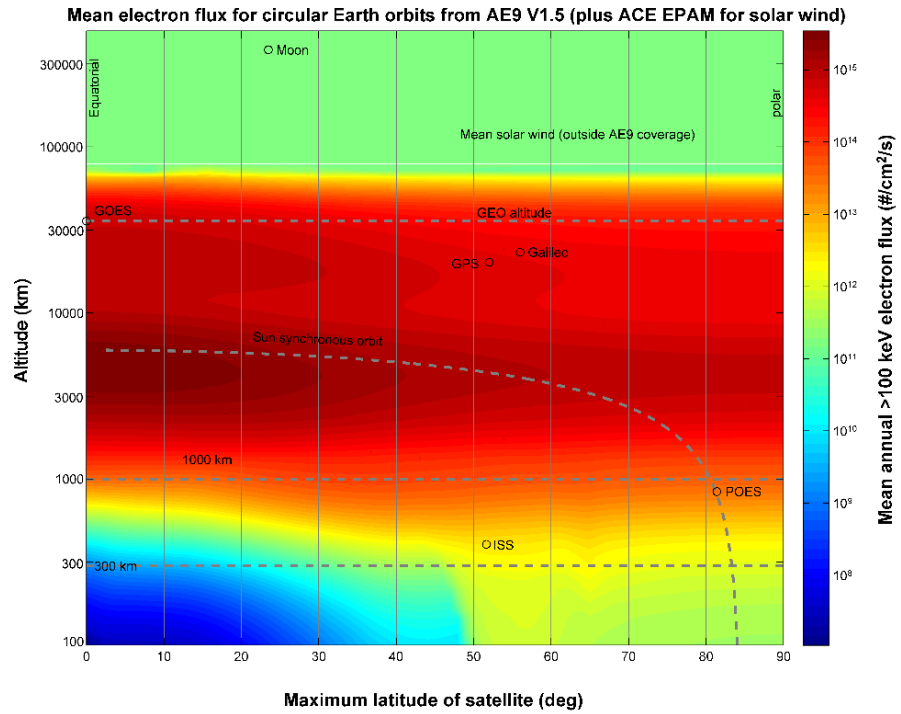


Figure 2: Electron flux model for circular Earth orbits<sup>5</sup>

Energy deposition destruction and its effect upon bombardment on the PI film depends on the mass of the particle. Protons are large particles over 1837 times heavier than an electron.<sup>6</sup> They deliver large amounts of ballistic energy over short distances in the material that is sufficient to break chemical bonds. The short depth impact displaces nuclei in the material and causes vibrational transitions responsible for separating bonds within the affected area.<sup>7</sup> In contrast, UV photons have no mass, yet are energetic enough to separate molecular bonds. The associated photo-oxidation reactions result in chain scission or crosslinking within the polymer chains. Low mass particles such as He<sup>+</sup> ions can break all chemical bonds along its track. Electrons are less massive particles that can rupture bonds with sufficient energy deposition. An electron passing through a polymer deposits energy in the material via coulomb repulsion, polarization, and electronic excitation. The nature of the electronic energy deposition leads to damage that is chemical bond selective.

Photons, protons, and electrons can also cause secondary electrons to be ejected and cause a charge imbalance near the surface. This is where it is important to distinguish between energy deposition and charge deposition.<sup>8</sup> Energy deposition refers to kinetic energy lost by a massive particle as it travels through a material, resulting in no net charge imbalance. Charge deposition results from a charged particle losing all of its kinetic energy while traveling through a material and the particle becoming embedded within the material, leading to a net charge imbalance.

When a disordered polymeric material is exposed to radiation, chemical bonds are broken, which can lead to crosslinking and chain scission. These phenomena are expected to affect tensile strength. The radiation type and dose rate influence the degree of crosslinking and the amount of chemical bond breakage. Previous studies suggest that if polyimide undergoes high electron irradiation doses, crosslinking will be prone to occur from recombination of reactive free radicals in the PI.<sup>9-10</sup>

The exact nature of the hazards on orbit depends on the space environment and the weather associated with a particular orbit. As electrons are the dominant source of damage in terms of energy deposition in Medium Earth Orbit (MEO) and GEO orbits, the mechanisms of electron-induced damage are most important in determining the long-term effects of space weather. This study focuses on the destructive processes that lead to chemical changes in Kapton film under high energy electron bombardment.

Previous studies show that electron irradiation of PI results in rupture of chemical bonds primarily in the imide ring and ether moieties, cross-linking, and radical formation.<sup>11</sup> Additionally, the damage caused by electron radiation results in an increased density of trap states in the material's bandgap.<sup>11</sup> The creation of new electron trap states in the material's bandgap can result in increased electrical conductivity (dark conductivity). As described by the study, this "dark conductivity" can increase by several orders of magnitude and is primarily because of the change in the chemical structure of the material, which gives rise to new electronic states that act as hopping sites for electrons. This is not to be confused with enhanced conductivity resulting from energy deposition as seen in the transient effect known as radiation-induced conductivity.<sup>12</sup>

There is evidence that high energy deposition can cause bond breakage. Also, if charge deposition builds up past the materials' dielectric breakdown potential, a discharge can occur, which may also lead to chemical bond breakage. ESD, as mentioned above, can be catastrophic and cause irreversible damage to the material and spacecraft components. Therefore, it is necessary to understand whether a given particle has sufficient energy to penetrate through the entire material.

One of the methods to ensure that any radiation-induced modification performed to the polyimide would reflect bulk material properties rather than the surface modification is to simulate the energy loss per unit length of the irradiated material at given energy of impinging electrons. **Figure 3** shows the results of a Monte-Carlo simulation performed with the Monte Carlo N-particle Code, v. 6.1 (MCNP6.1)<sup>13</sup> of energy loss per unit length for a 90 keV electron traveling through polyimide. Further, the energy of the electron beam was chosen such that the dominant form of damage would be a result of energy deposition rather than ESD as a result of charge deposition. The simulation included 20 million 90 keV electrons imposed on a 76  $\mu\text{m}$  thick Kapton film with an aluminum backing layer of infinite thickness. The simulation represented the average energy deposition per electron per 1  $\mu\text{m}$  thick Kapton. Results indicated that the average energy deposited per electron per  $\mu\text{m}$  is 1.08 keV. The NIST EStar database predicted an average energy deposition of 0.99 keV/ $\mu\text{m}$ .<sup>14</sup>

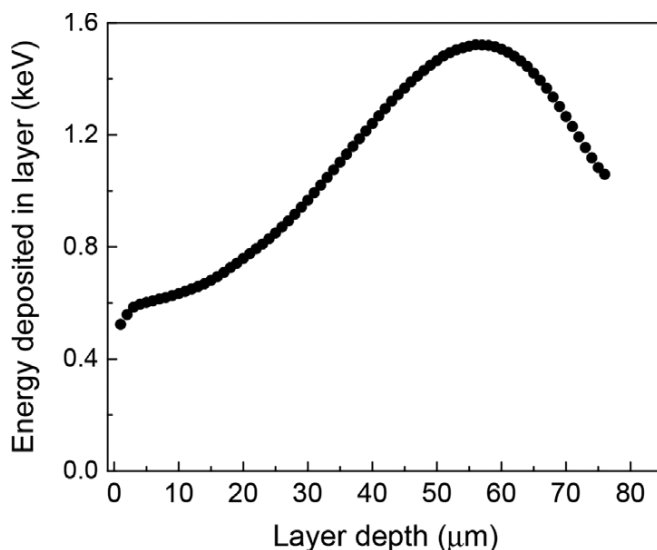


**Figure 3: Energy deposited in 76 μm thick Kapton by 90 keV electron beam<sup>15</sup>**

## 1.2 Healing after Electron Irradiation

After electron irradiation, the radicals that are formed as a result of chemical bond breakage can recombine, forming new chemical bonds. If those bonds are identical to the bonds that were originally broken, this phenomenon will result in a change of the material properties back toward those of the pristine material. We refer to this process as material healing. The rate and extent to which a material will heal depend on the particle species, dose rate, irradiation time, and the atmosphere it resides in. The previous study shows that the dark conductivity of PI falls off alongside of the radical concentration during material recovery.<sup>11</sup> As the dark conductivity values decrease back towards the pristine value, the radical concentration drops in a parallel form. The study concludes that the formation of free radicals is tied to the increase in dark conductivity of the material. The radicals may serve as small electron traps that increase the electron hopping probability across the material.<sup>16-18</sup>

The recovery of bulk properties of PI under exposure of specific gases was investigated and found that radical recombination occurred in the presence of O<sub>2</sub> and H<sub>2</sub>O but did not occur in the presence of N<sub>2</sub> or Ar.<sup>11</sup> PI will heal extensively if it is exposed to Earth's atmosphere (air). **Figure 4** represents the surface potential decay (SPD) measurements performed on the irradiated PI prior to air exposure and after exposure to each individual gas. SPD measurements are used to determine a number of physical parameters, including bulk conductivity, electron trap state density, and trapping and release rates for a material.

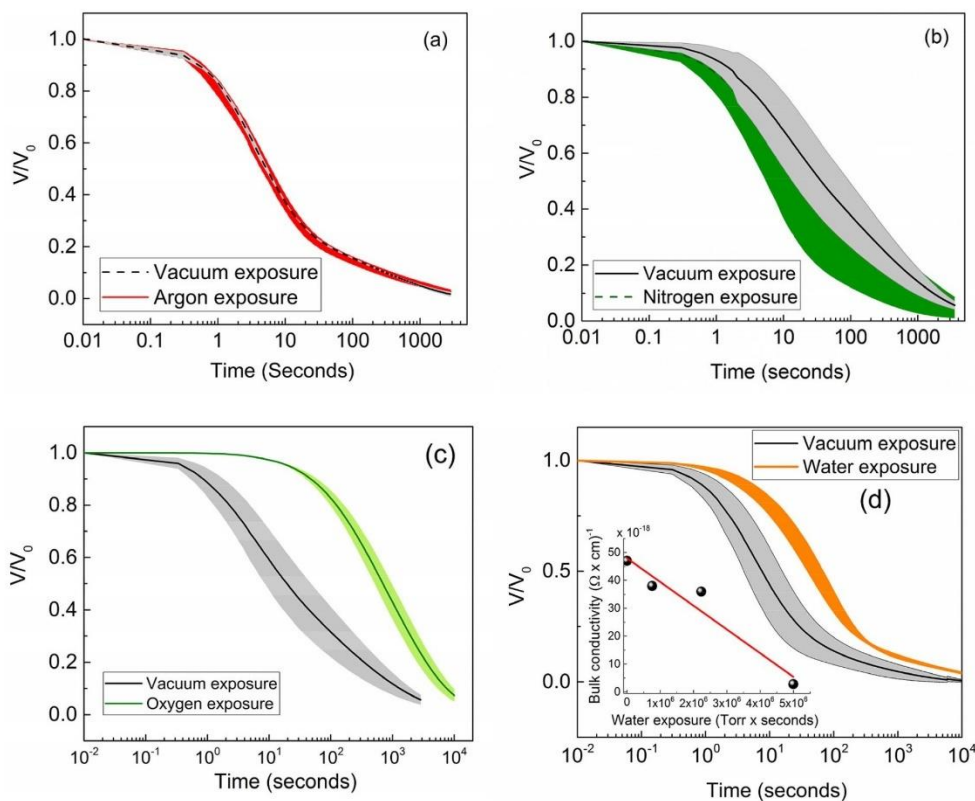


**Figure 4: SPD curves of PI samples measured before and after exposure of irradiated PI to partial pressures of (a) argon, (b) nitrogen, (c) oxygen, and (d) water vapor.<sup>11</sup>**

The phenomenon of reactant mediated radical recombination has been observed in other studies. The rate of self-reaction of peroxy radicals increases when exposed to  $\text{H}_2\text{O}$ .<sup>19</sup> Additionally, the reactions of alkyl and aromatic radicals with  $\text{O}_2$  have been well documented and are consistent with the behavior of electron-irradiated PI. The study suggests that oxygen-containing reactants are responsible for the material recovery under exposure to the atmosphere. These chemical interactions are explained by the reaction of alkoxy/peroxy radicals with oxygenated species in our typical environment.<sup>20</sup>

### 1.3 Motivation

Kapton has taken an honored place in the industry for space applications, aircraft, electronics, and even medical devices. Their exposure to irradiation-induced damage while a craft is on orbit drastically changes the Kapton's properties. This work reviewed the effects of electron beam irradiation on Kapton and potentially altering its electrical, chemical, or

mechanical properties permanently. The motivation includes the potential effects of surface charging and ESD that are associated with such a great dielectric. Additionally, the curiosity of material science has shown effective outbreaks from a trial and error methodology.

In the presented study, effect of fluorination on the physical properties of the electron-irradiated PI material was investigated. Fluorinated polymers are known to have a high thermal stability and chemical resistance. A common fluoropolymer with many applications is Polytetrafluoroethylene (Teflon). Teflon is typically used on non-stick pans because of its extremely low coefficient of friction and for situations that include corrosive materials. To access the modification of optical, charge transport, and mechanical properties of the PI due to the fluorine saturation, three experimental techniques were employed, namely, FTIR spectroscopy, conductivity measurements, and tensile measurements. Measurements were performed on fully recovered electron-irradiated PI, fluorine-treated, and pristine PI samples, with latter acting as a reference point for the study. It was experimentally impossible to perform the characterization techniques without any air exposure. All of the samples were exposed to air for at least 6 days in order to heal completely.

#### 1.4 Literature Review

Material enhancement may be beneficial or required for specific applications. Although Kapton is stable over a wide temperature range and heavily used in the space industry, there are ongoing studies to modify and improve the material. Most of these modifications are mainly performed at the surface such as one study achieved by chloromethylation followed by the azide decoration process, polyimide film aged under bipolar pulse voltage, and by plasma graft polymerization of vinylimidazole.<sup>21-23</sup> Manipulating and controlling the surface properties of Kapton without affecting its other outstanding properties is critically important. As previously mentioned, post-polymerization chemical modification may be restricted based on the complexity or cost of the process. For this reason, post-polymerization chemical modifications in Kapton are not common in the scientific community.

A recent study uses carbonization techniques to successfully create Boron-type functional groups in a Kapton-type polyimide film.<sup>24</sup> The further curiosity of the utility of post-polymerization bulk modifications led us to this study using electron beam irradiation. Irradiation effects on aromatic polymers have been studied by observing the gas evolution from

polymers during electron bombardment in vacuum including the effects of more massive particles such as ion irradiation on PI.<sup>25-26</sup> Lastly, molecular dynamic simulations have been produced to represent the effects of electron irradiation on a molecular level. These simulations predict a change in mechanical response of PI after electron induced damage.<sup>27-28</sup>

#### 1.4.1 Brush-type Surface Modification

Poly(methyl methacrylate) (PMMA) and polystyrene (PS) – brushed Kapton films were produced in a study.<sup>21</sup> The surfaces were activated by chloromethylation followed by the azide decoration process. Chloromethylation is the introduction of a chloromethyl group into a compound usually by use of formaldehyde and hydrogen chloride. A reaction mixture of chloroform, paraformaldehyde, and silicon and zinc chloride were stirred inside a flask containing a PI film. The reaction mixture is stirred for 6 hours at 50° C and then cooled at room temperature. The created PI films (PI-CH<sub>2</sub>Cl) were then washed with acetone several times and dried in a vacuum oven overnight. The azide decoration process involved the presence of excess NaN<sub>3</sub> while stirring the chloromethylated PI with Dimethylformamide (DMF). The reaction is again washed with acetone several times and dried in a vacuum overnight. **Figure 5** below visually represents the change in the chemical structure.<sup>21</sup>

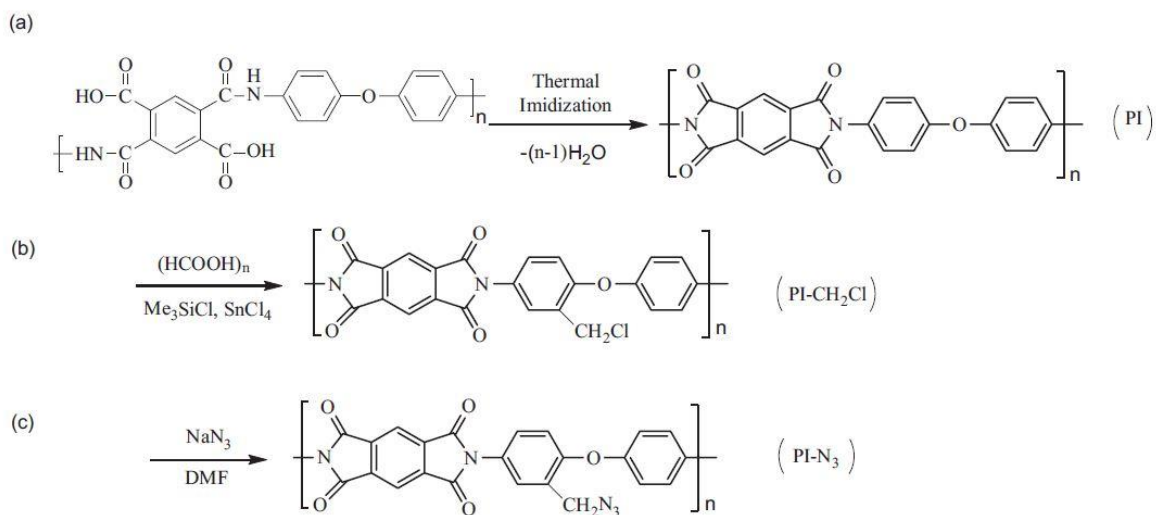


**Figure 5: Chloromethylation and azide decoration process<sup>21</sup>**

PI film surfaces were successfully prepared by chloromethylation and azide decoration under mild conditions. These surface changes made the production of PMMA and PS – brushed Kapton films possible.

#### 1.4.2 Electrical Aging in Polyimide

Another surface modification study uses Kapton 100HN films. The 50  $\mu\text{m}$  thick films used were aged under 3kV AC voltage.<sup>22</sup> The aging characterization was performed using dielectric measurements and FTIR spectra. The electric field gap was made up of a needle-shaped and one plate-shaped electrode. The needle-shaped was connected to the 3kV AC voltage, while the plate-shaped electrode was connected to the ground. The gap length between these electrodes was 2 mm.<sup>22</sup> The FTIR spectra shown in **Figure 6**, compared the relationship between pristine PI and different aging timed samples. The films were aged from 5 to 30 hours at the same AC voltage.

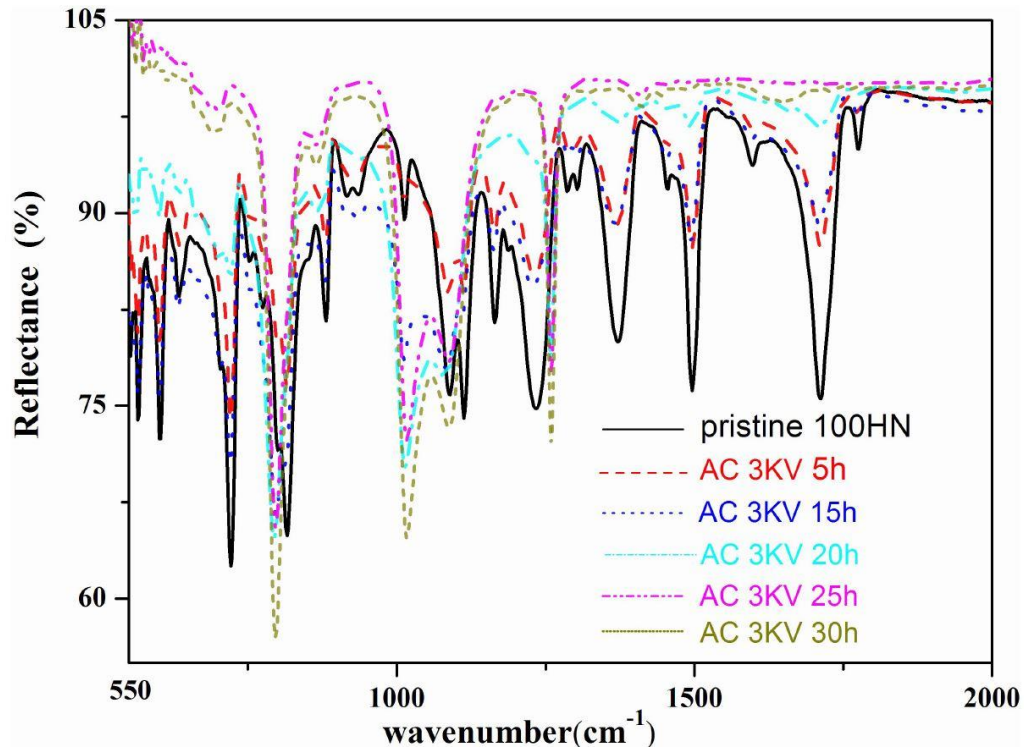


**Figure 6: FTIR spectra of pristine and aged 100HN PI at room temperature<sup>22</sup>**

The spectra clearly indicate that there were no chemical bond breaking for the samples that had a short aging time. Longer aged samples had hydrophobic C-H bonds and the amount of other important chemical bonds decreased. The hydrophilic OH groups increase as a result of aging. The autoxidation reaction is known to occur on the polymeric surface when oxygen is present. The ultimate products after the autoxidation reaction process are as follows,

Initial reaction:



Intermediate reaction:



R and R' indicate components of the polymer. During the material aging, ether linkage and C-H bonds in the aromatic rings are cut off and combined with the OH and OOH groups generated during the autoxidation reaction.<sup>22</sup>

#### 1.4.3 Improved Adhesion Techniques

Surface modifications have numerous objectives. In one study, surface modification was employed to improve adhesion between Kapton film and copper.<sup>23</sup> The film surface was modified by plasma graft polymerization of vinylimidazole. The film was exposed to 60 seconds of an argon plasma followed by periodic air exposure times of 5 to 10 minutes. The air exposure caused hydroperoxides, which can initiate the graft polymerization. Next, the argon treated film was submerged in an ethanol solution of vinylimidazole in which the dissolved air is removed by a repeating freezing-fusion procedure. After the graft polymerization, the film was washed with methanol dried under vacuum. Peroxide groups were generated at the surface of the film from the argon plasma and exposure to an air cycle. The surface roughness of the Kapton film increased significantly after the graft polymerization for 6 hours and even 24 hrs. Average height of the graft polymer was estimated at 22.5 nm. Finally, using the T-type peel strength technique, the peel strength was measured as a function of weight increased from the graft polymerization. The correlation is represented by **Figure 7**.<sup>23</sup>

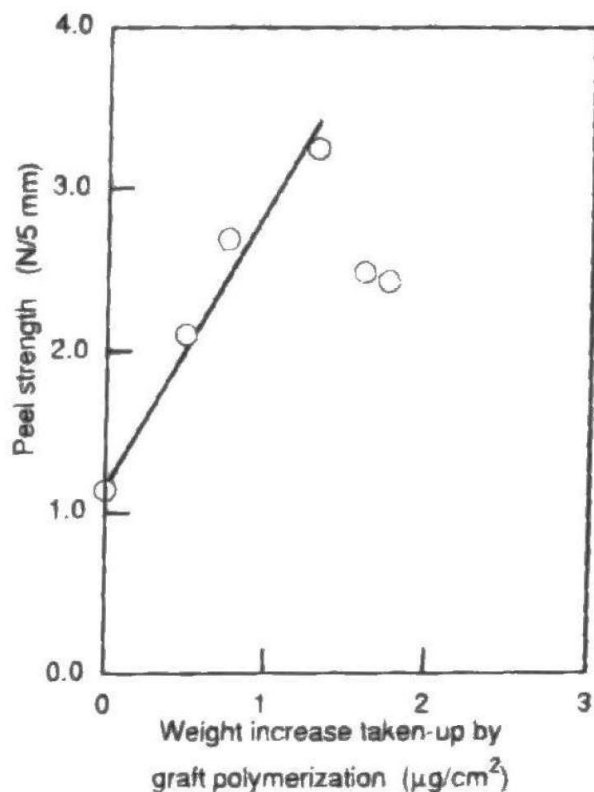


**Figure 7: Peel strength as a function of weight increased taken up by graft polymerization<sup>23</sup>**

The surface modification increased the peel strength and improved the adhesion between the Kapton film and the copper metal. The graft polymerization increased the peel strength by 2.9 times. The film surface achieved an island-sea type structure with every island height around 20 nm.

#### 1.4.4 Boron Bearing Kapton

Surface modification of polymers provides valuable improvements. It would then be worthwhile to study intermolecular changes. A previous study synthesized a Kapton-type PI film having boron-bearing functional groups.<sup>24</sup> The films carbonization/graphitization behavior was analyzed using X-ray photoelectron spectroscopy (XPS), scanning electron microscopy (SEM), X-ray diffraction (XRD), and Raman spectrometry. The boron doped samples were less conductive due to the hole carriers that were predominant to electrons. The electrical conductivity as a function of heat treatment temperatures for the samples is shown in **Figure 8**.<sup>24</sup>

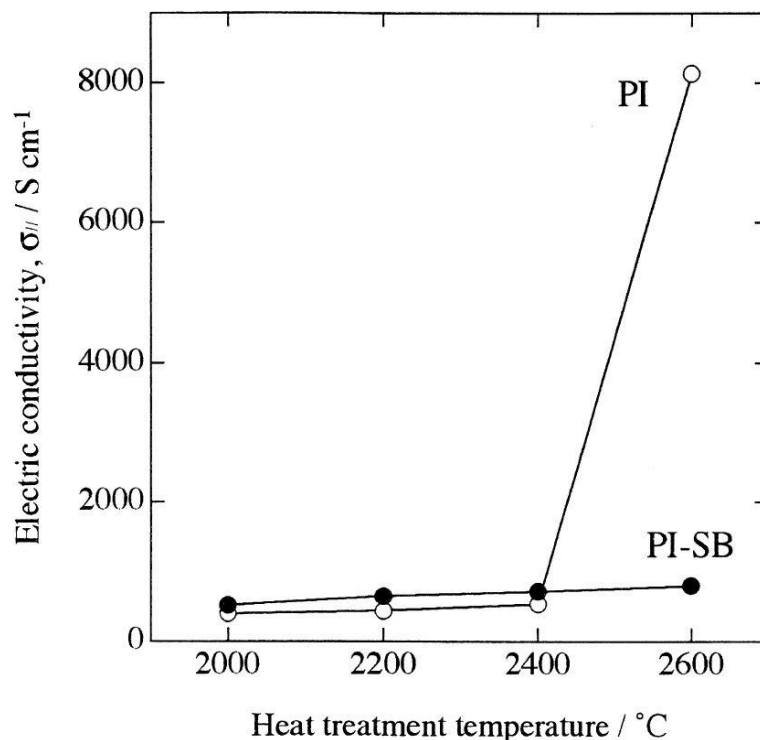


**Figure 8: Electrical conductivity of PI and PI-SB films measured at room temperature<sup>24</sup>**

Electrical conductivity for the boron-bearing PI dropped significantly. This may be beneficial for applications where a less conductive Kapton film is needed or lead to future experimentation where the enhanced sample is more conductive.

#### 1.4.5 Gas Evolution During Electron irradiation

A previous experiment that is complementary to the study described in this thesis measured irradiation effects of aromatic polymers and the evolved gases caused by the irradiation.<sup>25</sup> The Japan Atomic Energy Research Institute quantitatively measured the gas evolution during electron-beam irradiation of polyimides such as Kapton, Upilex-R, Upilex-S, poly(aryl ether ether ketone) (PEEK), poly(aryl ether sulphone) (PES), Udel poly(aryl sulphone) (U-PS), and poly(aryl ester) (U-Polymer). A steel vessel was designed to irradiate the samples under a vacuum of better than  $10^{-3}$  Pascal (Pa). The samples were placed in the steel vessel between two steel plates of thickness 50µm. The experimental diagram is shown in **Figure 9** below.

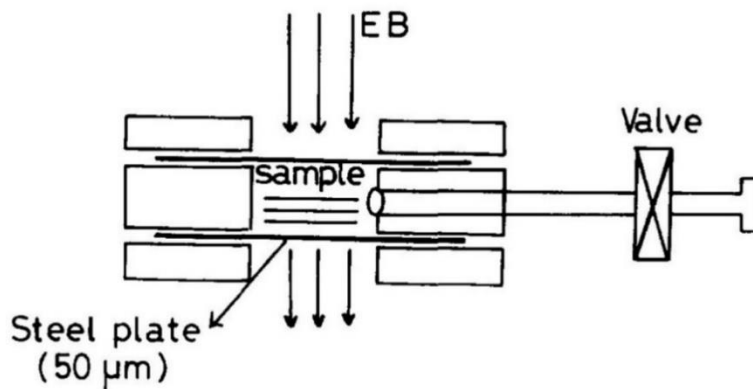


**Figure 9: Experimental setup of irradiated samples<sup>25</sup>**

The experimental data formulated the yield of evolved gases in moles per gram versus the dose rate in Gray ( $J \cdot kg^{-1}$ ) for each polyimide. Displayed in **Figure 10**, electron irradiation leads to the formation and release of several gases in aromatic polymers. The correlation between electron irradiation and gas evolution for Kapton is seen below.<sup>25</sup>

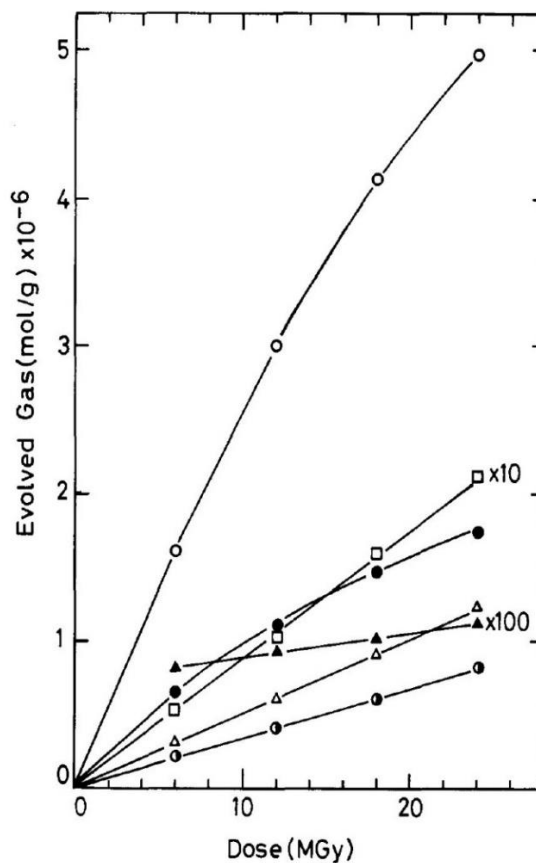


**Figure 10: Yield of evolved gases vs. dose for Kapton after electron beam irradiation: (O) total gas, (Δ) H<sub>2</sub>, (□) CH<sub>4</sub> (x 10), (●) CO, (•) CO<sub>2</sub>, and (▲) N<sub>2</sub> (x 100)<sup>25</sup>**

#### 1.4.6 Specificity of Ion Induced Damage

Similar to the effects of electron irradiation, energetic heavy ions can significantly affect the chemical composition of a material. FTIR absorption spectra for various polymers were compared in a study before and after the ion irradiation in vacuum.<sup>26</sup> Kr ions with an energy of 8.6 MeV/u were used to bombard the samples at a fluence of  $6 \times 10^{12}$  ions/cm<sup>2</sup>.

The study provided two key differences in the absorption spectra before and after irradiation. There was an overall increase in absorption intensity between 3800 cm<sup>-1</sup> and 2500 cm<sup>-1</sup> and an overall decrease in absorption intensity between 1600 cm<sup>-1</sup> and 500 cm<sup>-1</sup>. These changes were attributed to oxidative degradation.

#### 1.4.7 ReaxFF Simulations

ReaxFF simulations are a system of molecular dynamic simulations that have been developed to simulate large scale reactive chemical systems in a computationally practical way. The simulations are driven by force field calculations. ReaxFF uses a number of general relationships between bond distance, bond order, and bond energy to estimate the proper dissociation of chemical bonds to separated atoms. ReaxFF also implements Coulomb and van der Waals forces to describe non-bonding interaction between all atoms in the simulations. ReaxFF calculations have been successfully used to simulate large reactive systems of hydrocarbons.<sup>27</sup>

Recently this computational method has been adapted to simulate the chemical changes that occur when a slab of Kapton is bombarded by penetrating electron irradiation.<sup>28</sup> First, a large Kapton structure was formed and allowed to equilibrate. This represents pristine Kapton. It is impractical to simulate an electron moving through a material because the time step would have to be extremely short due to the high velocity of even a low energy electron. Therefore, electron beams were simulated by introducing a string of dummy atoms with no charge and no mass into random spots in the material. The slab and the positions of the electron “beams” are shown in **Figure 11**. These dummy atoms are completely unreactive with the system until their -1 charge is “turned on” for 2 fs, which simulates the passage of electrons through the material. While the electron charge is on, energy is deposited into the system via Coulomb repulsion, polarization and van der Waals forces, similar to real electron damage. The simulation is

allowed to continue for 0.5 ns, allowing the chemical damage resulting from the energy deposition to develop.

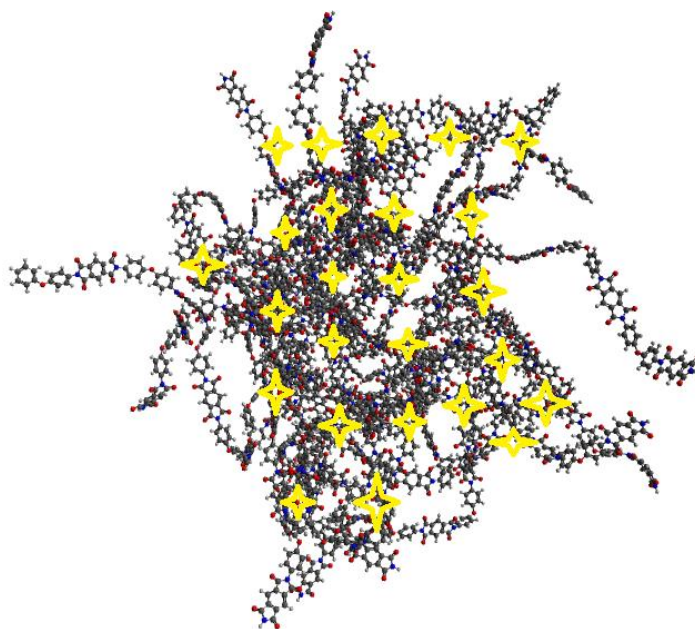


**Figure 11: Simulated Kapton slab and positions of “electron beams.” See text for further discussion.<sup>28</sup>**

The simulations find that the majority of chemical damage occurs in the imidic rings and ether moieties of the Kapton repeating unit (see **Figure 31**), leading to chain scission and crosslinking. Before electron irradiation and after the simulation has proceeded to completion, the system is “stretched” in order to calculate the stress/strain relationship of the pristine and damaged material, as shown in **Figure 12**.

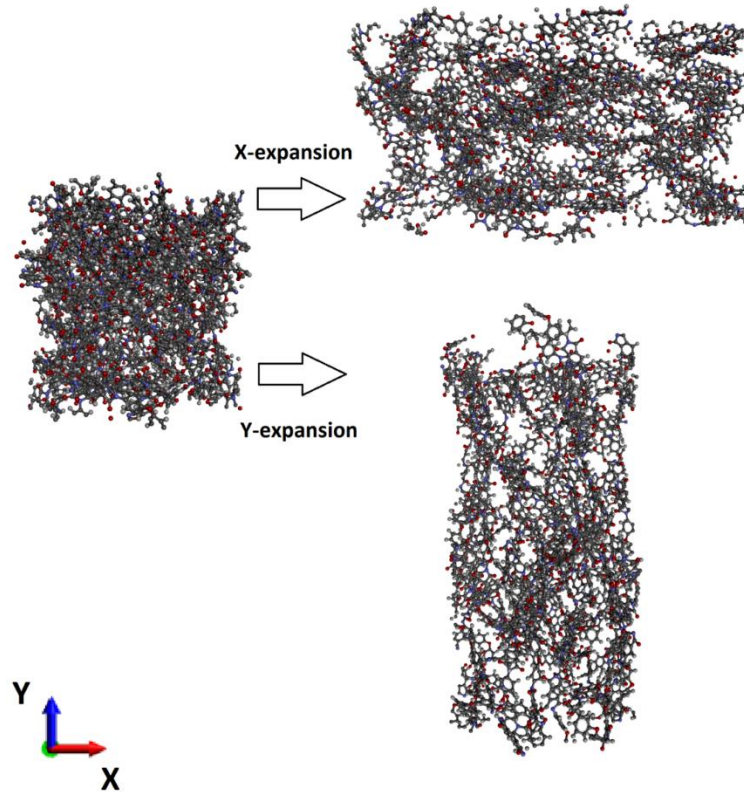


**Figure 12: Snapshots of the expansion of the polyimide in the X and Y directions in separate simulations<sup>28</sup>**

The resulting  $\Delta E$  - strain relationship is shown in **Figure 13** below. Clearly, the simulations indicate an increase in the material's Young's modulus after electron irradiation. A materials' modulus is retrieved from a stress – strain relationship. Therefore, it is important to understand the relationship between the change in energy,  $\Delta E$  (eV), and the stress applied. Equation 1 shows the direct unit conversion between a unit of energy per angstrom cubed to the unit of pressure used to represent stress, or GPa. Equation 2 shows the relationship between an angstrom and the representative size of the sample in inches.

$$1 \text{ eV}/\text{Angstrom}^3 = 160.21766208 \text{ GPa} \quad (1)$$

$$1 \text{ Angstrom} = 3.93701 \times 10^{-9} \text{ Inch} \quad (2)$$

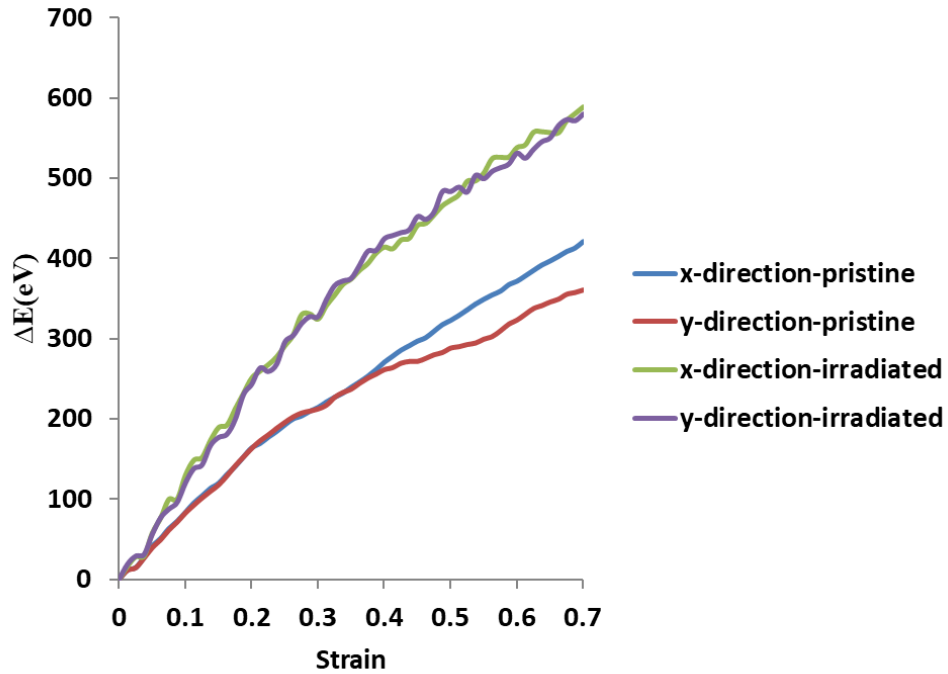


**Figure 13: Strain-stress graph of the polyimide slab before and after electron beam exposures as calculated using ReaxFF force field calculations.<sup>28</sup>**

The volumetric size of the Kapton slab sample used for these simulations were unknown. For the purpose of this study, the  $\Delta E$  – strain relationship is utilized as a comparative method to the experimental stress – strain relationship later seen in this thesis.

## Chapter 2: Experimental Procedures

The presented work utilized multiple specimens of 3 mil thick Kapton (76.2 microns). The pristine samples' only preparation procedure was vacuum baking along with the other two test films. This ensured the samples were clean and dry prior to any manipulation. The Binder vacuum drying chamber operated for 24 hours at ~150-200 torr and had a constant temperature of 65°C. The chamber pressure was regulated using a Pfeiffer vacuum pump. Experimental equipment used are shown in **Figure 14** and **Figure 15**.

Samples were irradiated with a mono-energetic beam of 90 keV electrons from a Kimball Physics EG8105-UD electron flood gun in the JUMBO space environment simulation chamber of the Spacecraft Charging and Instrument Calibration Laboratory (SCICL) at Kirtland Air Force Base in New Mexico, USA.

For each electron beam irradiation, a clean Kapton piece was mounted on a rotating “carousel” inside the vacuum chamber. The round aluminum wheel rotates while holding samples on the white rings. The Faraday cup, mounted in the center of the carousel, was used to record the flux with a very accurate measure compared to the absolute flux. This can be seen in **Figure 16**. During this experiment, the carousel's motion was locked in front of the electron gun to ensure homogeneity and repeatable raster among the samples. The beam raster is approximately 2.5 inches from the center of the wheel and focused around the center of the marked rings. A generous sized Kapton film was used for every electron aged sample and aged for approximately 40 hours. The time the material was aged ensured sufficient deposition throughout the entire bulk.



**Figure 14: Binder vacuum chamber**



**Figure 15: Pfeiffer vacuum pump**

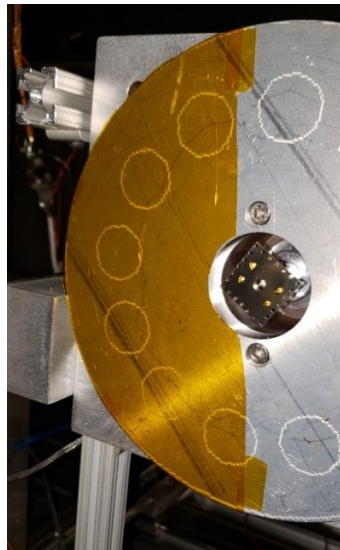


**Figure 16: Kapton sample mounted on the carousel**

**Table 1: Electron gun settings and Faraday cup readings**

Electron Gun	
Beam Energy	90 keV
Grid Voltage	0 V
Anode Voltage	300 V
Emission Current	21.1 – 32.5 $\mu$ A
Source Voltage	1.5V
Faraday Cup	
Electron flux	0.65 – 0.82 $\mu$ A

Electron gun settings from **Table 1** were kept constant for every run. The emission current recorded by the software varied from 21.1 to 32.5  $\mu\text{A}$ . This parameter was difficult to control and varied regardless of settings and initial warm-up procedures. The Faraday cup readings varied from 0.65 to 0.82  $\mu\text{A}$ . After the electron aging, the gun was turned off, and the chamber was prepared for air exposure. The electron aged samples were then placed inside the binder vacuum chamber after the aging procedure. Total dose for each sample was calculated by monitoring the flux on a Faraday cup mounted in the center of the carousel.

Fluorinated, or chemically enhanced samples, were produced similarly. After the aging process of the film was completed the chamber was flooded with Trifluoromethane, or fluoroform. Approximately 48 hours later, the fluorinated sample was removed from the chamber and placed alongside the electron irradiated samples in the vacuum oven.

Electrical conductivity analysis was conducted using a resistivity test fixture designed to satisfy the ASTM D257 standard. This method of characterization is used to understand how the material behaves when an electric current is applied through the material. The test measures the electron conductivity in the pristine and processed samples. This property is particularly important for space-based and electronic applications of the film.

The FTIR absorption spectra of the samples are used to identify and differentiate between the chemical bonding and vibrational modes of the materials. The spectrum of each sample is used to differentiate between the materials at a molecular level by indicating the individual chemical bonds in each material. Changes in the relative peak height or the appearance/disappearance of peaks indicate chemical changes as a result of the electron and chemical treatments. These tests characterize the chemical changes that occurred during the irradiation and post-polymerization chemical enhancement techniques applied in this study.

Mechanical analysis of the film samples compares the mechanical properties of the films before and after post-polymerization modification. The procedure determined if changes after modification are mechanically advantageous for a given application. These factors include a change in the samples' tensile strength, ductility, or the ability to withstand plastic deformation. Additionally, the analysis determines mechanical property changes when exposing the material to high energy electrons. The bombardment is subject to create chemical bond breakage that will affect the molecular alignment of the material, polymer chain length,

and degree of crosslinking. All of these chemical effects lead to changes in the material's mechanical properties.

## 2.1 Jumbo Vacuum Chamber

The Jumbo vacuum chamber, shown in **Figure 17**, is a 1.8m by 1.8m cylindrical chamber that was used for this experimental study. The chamber is inside the Spacecraft Charging and Instrumentation Calibration Laboratory (SCICL) in the Space Vehicles Directorate of the Air Force Research Laboratory (AFRL) at Kirtland AFB.



**Figure 17: Jumbo Environmental Simulation Chamber<sup>29</sup>**

The chamber has ports and feedthroughs that assist with mechanical, gas, and electrical applications. The completely dry-pumped chamber keeps test materials clean and with minimal surface contamination. Initially, the chamber is pumped using an Alcatel ACG 600 which consists of a dry multi-stage roots pump and a roots blower. The peak pumping speed of this rough pump is 8000L/min and can pump the chamber from atmospheric pressure to rough vacuum ( $10^{-3}$  torr) in fifteen minutes. Next, the chamber is pumped using a two-stage Sumitomo Marathon CP-20 cryo-pump operating at 13 Kelvin (K). The cryo-pump has a pumping speed of 582,000 L/min through a 20" aperture. It will take the chamber from the ending rough vacuum ( $10^{-3}$  torr) to high vacuum ( $10^{-6}$  torr) in fifteen minutes. The last pumping device used is an oil-free 18" Mitsubishi FT3301W turbo-molecular pump. The turbo has a pumping speed of 360,000 L/min and is backed with a 600L/min Varian tri-scroll dry pump.

The turbopump would be able to bring the chamber to high vacuum on its own in several hours. It is primarily used when gas is flowing into the chamber to avoid saturation of the cryopump.<sup>29</sup>

Jumbo contains a thermal stage that can be cooled down to liquid nitrogen (LN<sub>2</sub>) temperatures and heated to 80° C. The inner sample mounting stage is held perpendicular to the chambers' incident beams. Grazing incident angles can be achieved by swiveling the stage. While not used for this study, the chamber is also equipped with a three-axis translation stage providing a platform for various sensors and sample holders. The sample carousel used in this study may be moved closer to the location of electron, ion, and VUV sources. This is necessary to have some degree of control over the beam size and flux by taking advantage of geometric arrangements.

The space environment is complex and has unpredictable energetic particles that can range in energy and flux over many orders of magnitude. Therefore, it is impossible to simulate all of the parts simultaneously. Several tradeoffs must be made to have a productive and practical simulated environment. The chamber focuses the electron and photon environment of GEO and the electron, photon, and ion environment of LEO.

The electron source comes from a Kimball Physics EG8105-UD electron flood gun with a range of 1keV-100keV. There are two main functions of the gun. First, the 20keV beam injects shallow penetrating electrons into thin test materials acting as a charging source. Flux settings can be controlled from pA/cm<sup>2</sup> to tens of nA/cm<sup>2</sup>. As a reference, low fluxes (50 pA/cm<sup>2</sup>) of 20keV electrons are used to simulate the typical flux seen in GEO.<sup>4</sup> The rate of these fluxes charge the samples so that they reach equilibrium in several hours. This time frame allows the operator to capture the underlying physics. Without focusing the beam, it comes out of the gun at 20keV and a low divergence of <5°. A raster mode is required in order to provide uniform exposure. The non-uniform exposure on the experimental sample later seen in this study is not a divergence problem but a geometric one where the sample was not in the beam path. Lastly, the electron gun is capable of running in a pulse mode, not used for this study.

The instrumental error of the electron gun is the largest concern for the study at hand. The electron flux vary around 30% and can be improved by warming the gun for several hours. **Figure 18** below represents the electron beam flux at 90 keV with rastering as a function of time.<sup>29</sup>

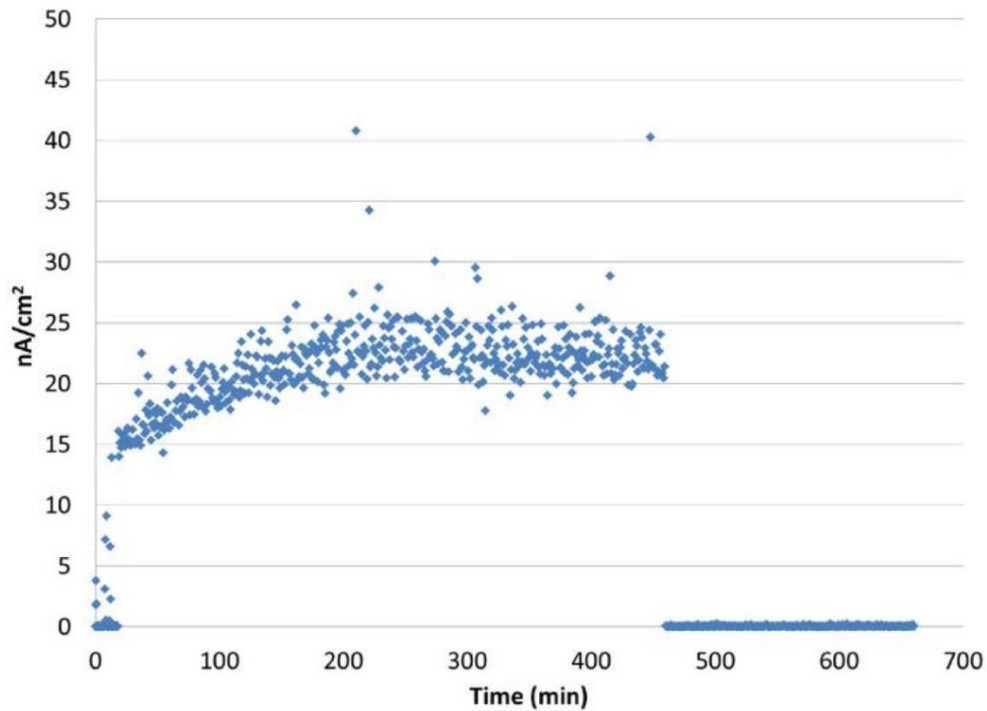


**Figure 18: Electron beam flux at 90 keV with rastering as a function of time<sup>29</sup>**

## 2.2 Electrical Conductivity

Electrical conductivity measurements are a useful method to probe changes in PI structure due to irradiation. Conductivity is the ability of all materials to pass an electric current.<sup>30</sup> **Figure 19** represents a simple conductor of length  $L$  and resistance  $R$ .

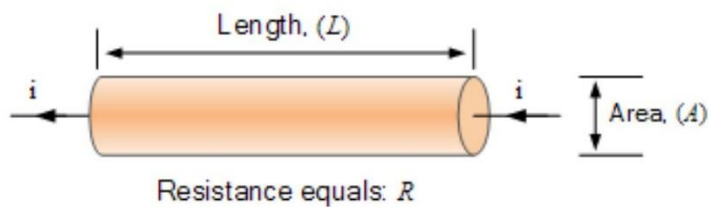


**Figure 19: A Single Conductor<sup>31</sup>**

The current,  $I$ , flowing through the conductor is represented by Ohm's Law (Eqn. 2). The current is equal to the voltage ( $V$ ) over the resistance ( $R$ ). The resistance is directly proportional to the length of the rod.

$$I = \frac{V}{R} \quad (2)$$

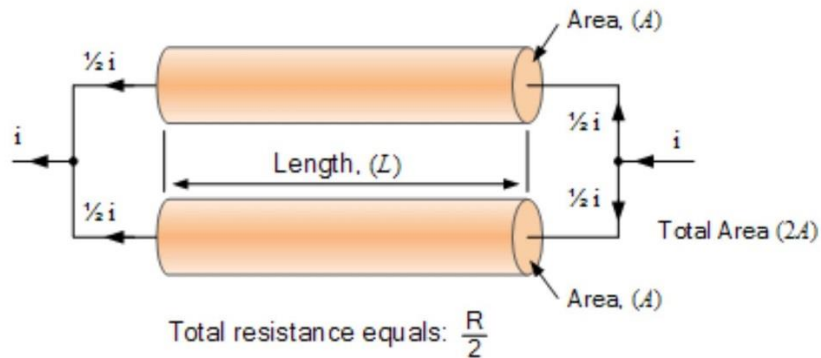


**Figure 20: A Double Conductor**<sup>31</sup>

If a second rod is added as in **Figure 20** above, the effective area,  $A$ , is doubled. However, having the two conductors in parallel has effectively halved the current. Therefore, the resistance is inversely proportional to the cross-sectional area,  $A$ . It is shown as the effective length,  $L$ , over the area.

$$R \propto \frac{L}{A} \quad (3)$$

Additionally, the resistivity depends on the material itself. A proportionality constant or resistivity,  $\rho$ , gives rise to the electrical resistivity equation.

$$R = \rho \frac{L}{A} \quad \text{or} \quad \rho = \frac{RA}{L} \quad (4)$$

Since conductance is the reciprocal of resistance, conductivity ( $\sigma_c$ ) is the reciprocal of resistivity.

$$\sigma_c = \frac{1}{\rho} \quad (5)$$

The model 8009 resistivity test fixture, by Keithley Instruments, Inc., connected to the Model 6517 Electrometer/High Resistance Meter employs the ASTM (American Society for Testing and Materials) standard D257.

The standard states that volume resistivity ( $\rho_v$ ) is calculated from Eqn. 6.

$$\rho_v = \frac{K_v}{t} R \quad (6)$$

where  $K_v$  is the effective area of the guarded electrode for the particular electrode arrangement employed. This effective area is divided by the average thickness of the sample,  $t$ , and multiplied by the volume resistance in ohms ( $\Omega$ ),  $R$ . The Model 8009 uses circular electrodes.  $K_v$  is then calculated from Eqn. 7.

$$K_v = \pi \left( \frac{D\emptyset}{2} + \beta \frac{g}{2} \right)^2 \quad (7)$$

The effective diameter of the guarded electrode,  $D\emptyset$ , is 5.40 cm or  $2\frac{1}{8}$  in. The effective area coefficient is  $\beta$ , and the distance between the guarded electrode and the ring electrode,  $g$ , is  $\frac{1}{8}$  in.

To simplify,  $\beta = \emptyset$ , and  $K_v$  is represented by Eqn. 8.

$$K_v = \pi \frac{(D\emptyset)^2}{4} \quad (8)$$

Therefore,

$$K_v = \pi \frac{(5.40 \text{ cm})^2}{4} = 22.9 \text{ square centimeters}$$

Plugging in the value for  $K_v$  in Eqn. 6, we get a simplification of volume resistivity where  $t_c$  is the average thickness of the sample in centimeters.

$$\rho_v = \frac{22.9}{t_c} R \quad (9)$$

From Eqn. 2, or Ohm's law,  $R$  can be replaced by divided the applied test voltage by the subsequently measured current.

$$\rho_v = \frac{22.9V}{t_c I} \quad (10)$$

However, despite the simplicity of ASTM method, the charging behavior of a polymer used as a surface material for a spacecraft on orbit can be more accurately described by the using the SPD method, which utilizes charge injection similar to typical spacecraft operating conditions.<sup>32</sup> The SPD method is performed under a well-controlled vacuum environment over a longer time scale (days in some cases). The latter is necessary for accurate observation of charged particle transport through PI without obfuscation by short-term molecular polarization current or charge injection at the electrode interface.

**Figure 21** represents a charge/discharge curve of PI material that is formulated from SPD measurements. The density of trapped states can be extracted from region I where the charging beam is always on. There are two other useful material parameters that may be extracted from a material's charge/discharge curve when the discharge beam is off. First, the electron mobility and trapping and de-trapping rates are retrieved from region II. Next, dark resistivity and conductivity of the material can be retrieved from region III. The models and measurements by Song *et al* are used to estimate electrons emitted per incident electron to formulate the charge/discharge curve.<sup>33</sup>

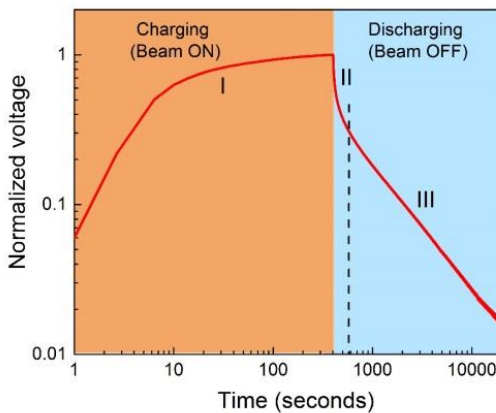


**Figure 21: Representative charge/discharge curve of PI material bombarded with non-penetrating electrons. Shaded areas represent the three regions of the charge/discharge curve.<sup>32</sup>**

Electrical conductivity analysis was conducted using a resistivity test fixture designed to satisfy the ASTM standard, due to the unavailability of SPD set up during this study. We understand, however, that conductivity values measured by ASTM may not be fully conclusive.

Electrical conductivity measurements were measured using the aforementioned model 8009 resistivity test fixture by Keithley Instruments, Inc. The test fixture is connected to the 6517 electrometer/high resistance meter and operated via a LabView program. The experimental setup is shown in **Figure 22** below.



**Figure 22: Electrical conductivity measurement test setup**

The PI films are placed in between the two electrodes. The film samples are within the sample size to make sure there are no conductive paths between the electrodes other than through the sample. **Figure 23** shows a pristine sample of Kapton centered before closing the lid and securing the latch. The front of the test fixture has a resistivity button that was pushed in to measure volume and not surface resistivity.



**Figure 23: 3"x 3" pristine Kapton sample on the test fixture**

The program supplies the specific current reading measured through the material as a function of time. First, a voltage range is selected before the test voltage is applied to the insulator sample. The program has two options of 100 V and 1000 V test ranges. The test voltages used for these ranges are 50V, 100V, 250 V, 500 V, 750 V, and 1000 V. The current measurement range is most accurate at the most sensitive setting. The model is then placed in auto-range to achieve this.

When the program is set to run, it begins to record the current reading levels before the voltage is turned on. As seen in **Figure 24** below, these readings vary significantly and do not exactly oscillate around zero. Then the voltage is turned on for 60 seconds, depicted by the abrupt spike in the graph, while current readings are constantly recorded. The time the specified voltage is applied is called the electrification time. Current readings are terminated after the end of the electrification time.

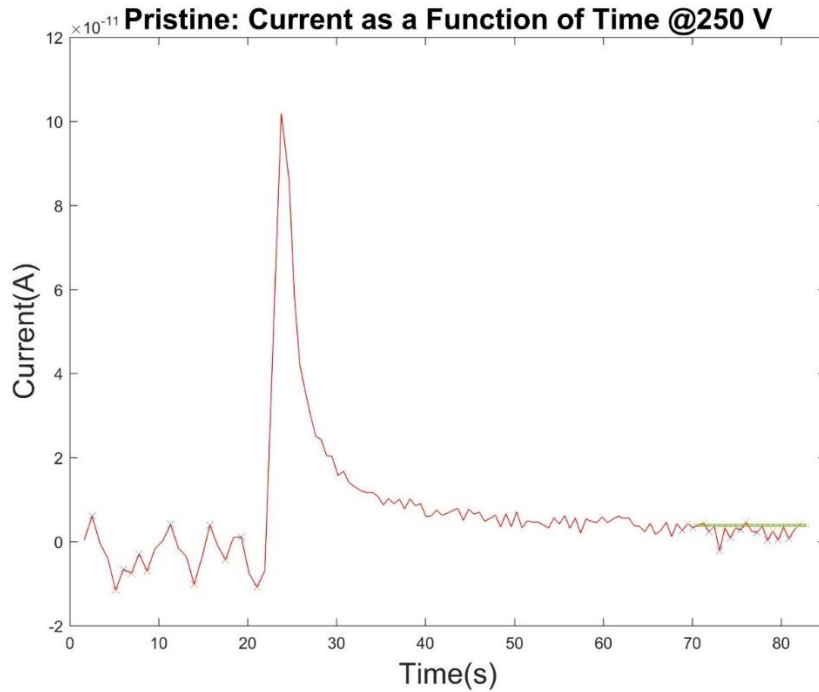


**Figure 24: Current as a function of time performed at 250V for the pristine sample**

The initial offset readings are a product of ground-level readings close to the lower end of the detection limit, a previous sample stored test charge, or simply systematic error in the experimentation device when close to the detection limit. Additionally, the converging current has a deviation of its own. The data is statistically retrieved using the following process. First, the amplitude of the ground level readings is determined. The offset or difference from zero is applied to the amplitude of the converging current values during the electrification time. This new current shift is seen in **Figure 25** below. Statistical error bars were applied to the converging current readings using the standard deviation of the mean (SDOM) for the set of data points.

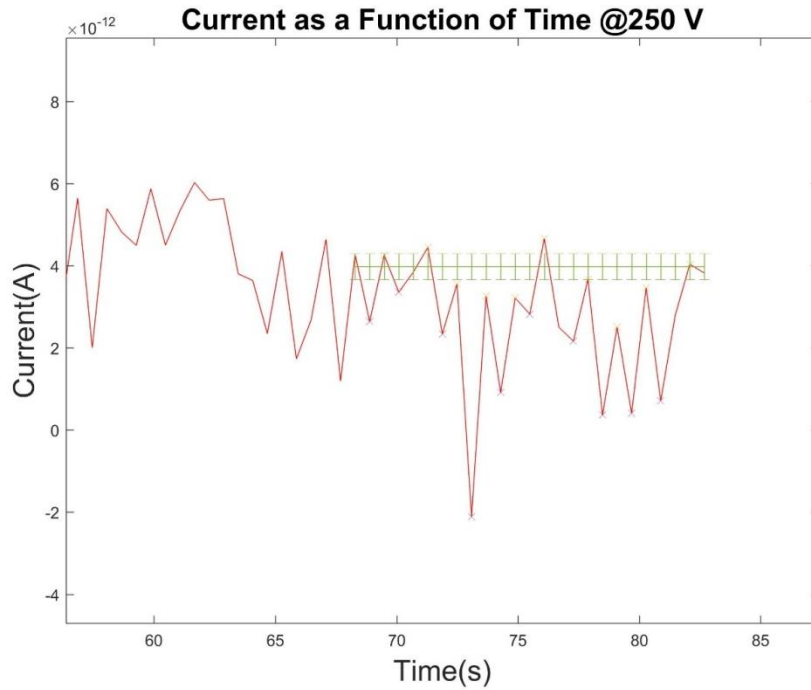


**Figure 25: Current as a function of time performed at 250V for the pristine sample; statistical error bars**

The SDOM (Eqn. 11),  $\sigma_{\bar{x}}$ , uses the standard deviation  $\sigma_x$ , which characterized the average uncertainty of the separate data points, divided by the square root of N number of data points.

$$\sigma_{\bar{x}} = \sigma_x / \sqrt{N} \quad (11)$$

As N increases the SDOM would slowly decrease. This decrease is expected since more measurements would naturally expect for the final result to be more reliable.<sup>34</sup>

### 2.3 Spectroscopy

Spectroscopy dates back to Sir Isaac Newton’s experimentation. Although forms of refraction of light had been previously seen, he was responsible for establishing mathematical rules for the refraction of light.<sup>35</sup> The experiment involved sunlight coming into a dark room through a hole and passing through a prism. The light then passes through the second prism to produce a selected color spot. **Figure 26** shows an example of the experimental setup used by Newton to study light refraction.



**Figure 26: Newton studying the refraction of light**<sup>35</sup>

This work initiated by Newton was continued by Frederick William Herschel. He believed that there were other components of sunlight outside the visible region. Using an experimental setup similar to that pictured in **Figure 26** he placed a blackened bulb underneath the red color and the temperature of the bulb increased to room temperature. This increase in temperature was evidence that the bulb was absorbing radiation that is invisible to the human eye. He called this portion of the electromagnetic spectrum infrared. A future discovery was made when he placed a sample in the path of the infrared light. The reference temperature changed as the sample passed through different points in the spectrum. It was concluded that at these points the sample absorbed infrared light. Infrared spectroscopy was born and defined as the “measurement of light absorbed in the infrared.”<sup>35</sup> Additionally, experimentation led to conclude that the absorption was proportional to the difference between the reference temperature and the temperature at different parts of the spectrum.

IR spectroscopy is the study of the interaction of radiation with molecular vibrations. Electromagnetic radiation can be absorbed by material if there is an energetic transition in the material of the same energy (or unit multiple) as one photon of light. **Figure 27** shows the molecular effects associated with the different wavelength regions. Photons in the IR region are resonant with excitation of molecular vibrations. Upon absorption of an infrared photon, a specific chemical bond will be excited into a higher vibrational energy level. Each chemical bond has a slightly different energy and therefore corresponds to the absorption of one discrete energy of infrared radiation.

Two important components for a bond to absorb IR radiation are radiation frequency and the molecular dipole moment. A resonance condition occurs when the oscillating radiation frequency matches the natural frequency of the particular mode of vibration in the molecule. Next, this vibration must cause a change in the dipole moment of the molecule.<sup>36</sup> Then and only then, will the molecule absorb the emitted photon.

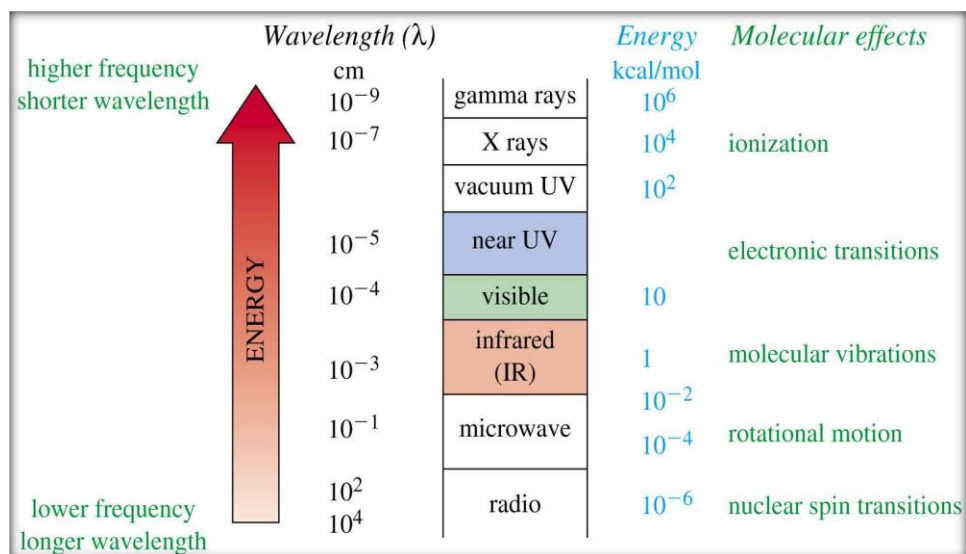


**Figure 27: Energy, Wavelength, and Molecular Effects<sup>37</sup>**

The vibrational state change is simply the increases in energy associated with a particular molecule. The vibrational energy level changes from a ground to an excited state. This energy absorption corresponds to specific modes or combinations of atomic movements. These movements result in a change of bond angle or bond length, during in and out of plane motion. Several possible vibrational modes are illustrated in **Figure 28**.

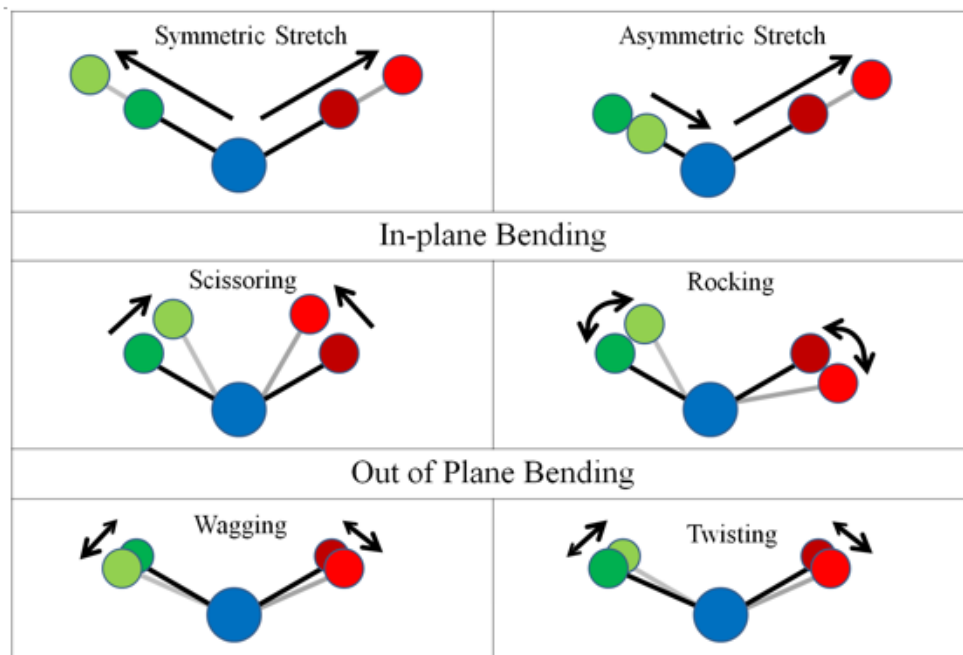


**Figure 28: Stretching and bending vibrations in molecules<sup>38</sup>**

The IR vibrational bands are characterized by the frequency (energy), intensity, (polarizability), and the band shape (chemical environment of bonds).<sup>36</sup> These regions of absorption and transmission make up the spectrum which can be used to identify and analyze samples. The spectrum is represented as percent transmission, or absorption, and is a function of the frequency of radiation in terms of wavenumber. The spectrum can be divided into two regions: the fingerprint and the functional group region with wavenumbers 1500-400 and 4000-1500, respectively. An example of Hexane in **Figure 29** below differentiates between these regions.

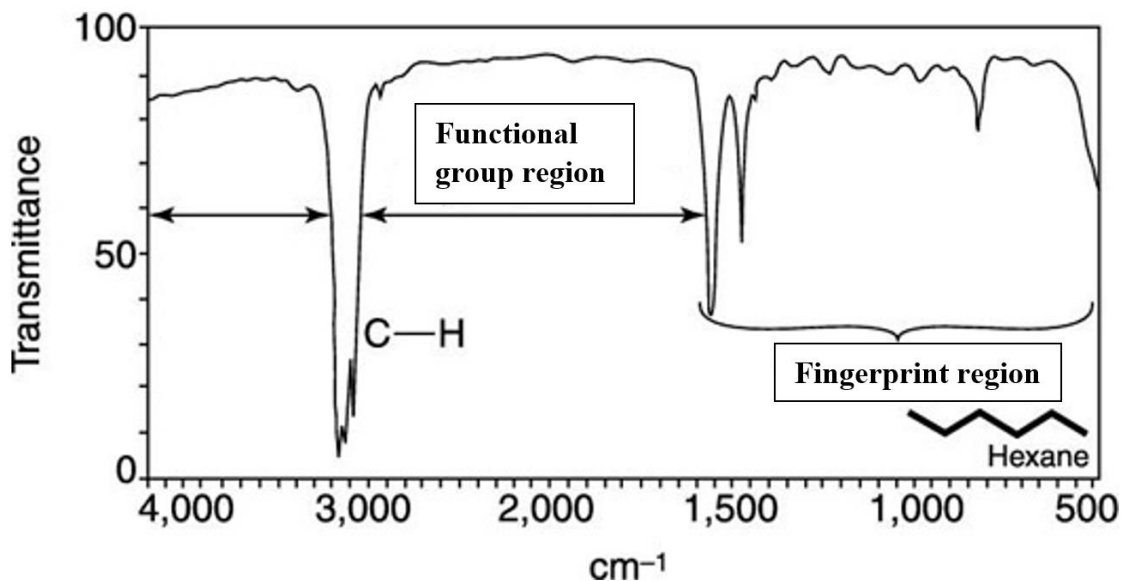


**Figure 29: FTIR spectrum of Hexane<sup>39</sup>**

The fingerprint region is unique to each molecule and corresponds to the molecule as a whole. It depends on the masses of the atoms, their geometric arrangements, and the strength of the chemical bonds. The functional group region shows the characteristic vibrations of particular groups. An example is the phenyl ring C-H stretch seen in the ~3000-3100 assignment above.

Phenyl rings are similar to benzene minus the hydrogen, which can be replaced. It serves as a functional group when replaced with some other element or compound. Six carbon atoms are bonded together in a hexagonal planar ring shown in **Figure 30**.

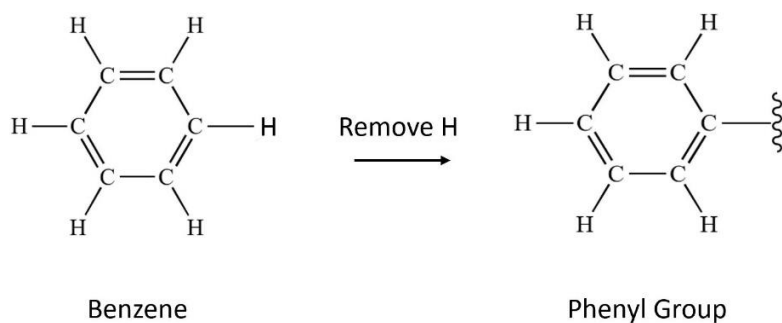


**Figure 30: Benzene and Phenyl group molecular structures<sup>40</sup>**

The phenyl group is common in organic chemistry and is present in the chemical structure of Kapton displayed in **Figure 31**. Kapton-H<sup>®</sup> is a polyimide film (PI) developed by DuPont in the late 60s. The process involves the condensation of pyromellitic dianhydride and

4,4'-oxydiphenylamine. Pyromellitic dianhydride is an organic compound that is used to prepare polyimide polymers like Kapton. Poly-oxydiphenylamine is used as a cross-linking agent for polymers.<sup>41</sup> The step polymerization process uses reacting monomers to create polymer chains.

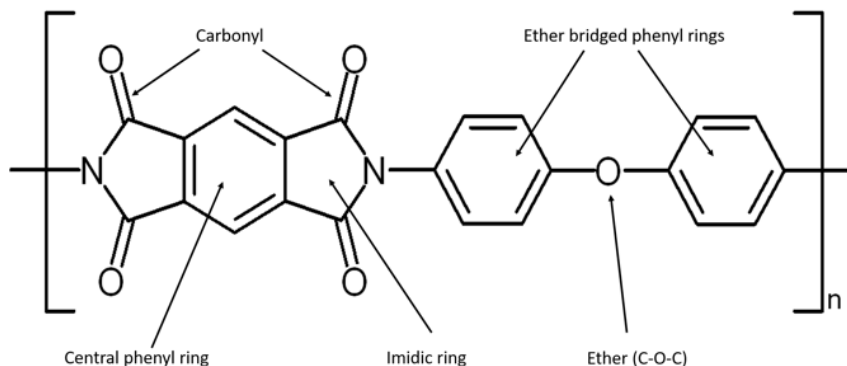


**Figure 31: Kapton chemical structure: poly-oxydiphenylene-pyromellitimide<sup>42</sup>**

The first-generation IR spectrometer was invented in the 1950s. The monochromator used was a prism optical splitting system made out of sodium chloride. This device transmits narrow bands of wavelengths of light. The scan range and repeatability of the system was poor. In addition, the requirements for the sample were strict. The spectrometer performance led to the second-generation IR spectrometer a few years later. This monochromator used gratings responsible for splitting and refracting light into several beams when traveling in a specific direction. Although it was much better compared to the first-generation spectrometers using prism monochromators, the low sensitivity and accuracy led to the third generation used today.<sup>43</sup>

FTIR spectroscopy uses an interferometer instead of a monochromator. This device merges two or more sources of light, as seen in **Figure 32** below. The interference is then used to make precise measurements. Compared to the first generations of spectrometers, this device is exceptionally better.

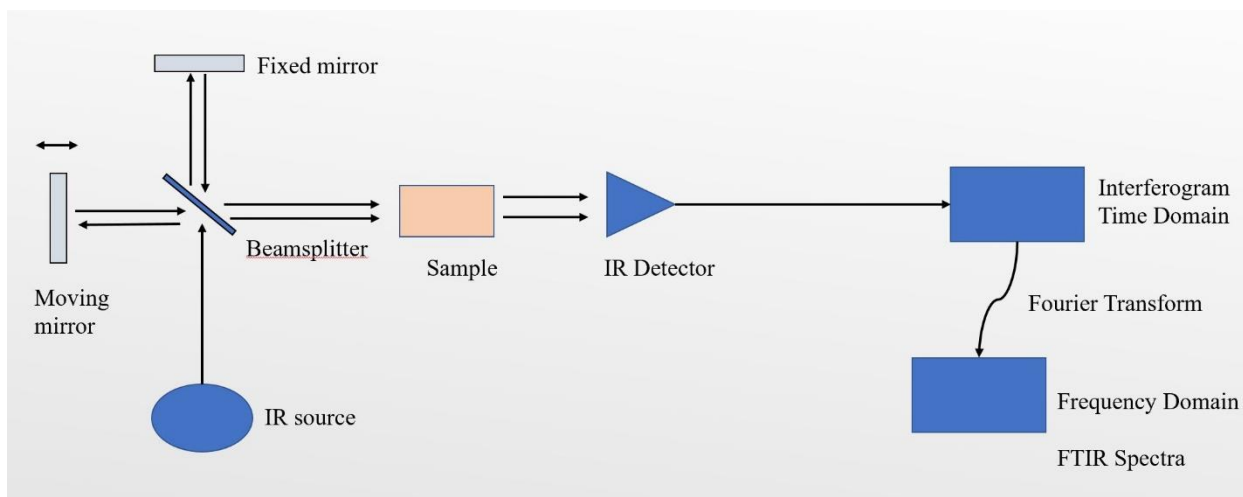


**Figure 32: FTIR design schematic**

The Michelson interferometer receives the IR source and splits the beam of light in two. If both mirrors were fixed, the light beams have traveled the same distance, otherwise known as the zero- path difference (ZPD). The moving mirror accounts for a difference in distance traveled known as the optical path difference (OPD). The OPD is multiples of the wavelength that causes constructive interference between the light waves. Destructive interference occurs when the path difference is multiples of the half wavelengths. The moving mirror causes the intensity of the signal to be between maximum and minimum.<sup>43</sup> The light is transmitted through the sample and to the IR detector. This increase and decrease in the signal recorded at the detector create a cosine wave called the interferogram. This time-dependent function records the brightness of the transmitted light as a function of time. This type of spectrum is commonly referred to as being in the time domain. By applying a Fourier Transform, one can decompose a signal in the time domain into its constituent frequencies. The new frequency resolved signal is commonly referred to as being in the frequency domain. The frequency domain infrared absorption spectrum can be used to identify the absorption or transmittance of all liquid, gas, and solid samples as a function of photon energy, in reciprocal centimeters (commonly referred to as wavenumber). The mid-IR range refers to radiation between  $4000 \sim 400 \text{ cm}^{-1}$ . This infrared region covers the absorption of the individual chemical bonds that make up most organic compounds and inorganic ions.<sup>43</sup>

Kapton film samples were investigated chemically using their FTIR spectra. The spectra were obtained by a Nicolet 6700 FTIR spectrometer with reflection mode in the  $400 \text{ to } 4000 \text{ cm}^{-1}$

range. The instrument setup is shown in *Figure 33*. The samples were analyzed at  $2\text{ cm}^{-1}$  resolution and averaged for 32 scans. The background of the atmosphere was measured and automatically subtracted from the spectrum.



**Figure 33: The Nicolet 6700 experimental setup (Left); Sampling plate (Right)**

The detector used was a liquid nitrogen cooled mercury cadmium telluride (MCT) with a KBr beam splitter. The spectral range configuration of both the detector and beam splitter overlap to cover the mid-IR region. The sample plate holds the diamond crystal where the sample is held. The swivel pressure tower closes in on the sample and pinches it down with the pointed powder tip.

The OMNIC spectroscopy software was used to collect the background and spectrum scans of each sample. Initially, the pressure tower was placed close enough to the diamond crystal such that a background scan can be retrieved. The software then proceeds to ask the user to place the sample desired to collect a spectrum from. The process with a new background scan was used for all three PI samples. **Table 2** below was used to identify some of the characteristic vibrational assignments of the experimental samples. Each peak corresponds to a specific vibrational mode of one bond within the monomer. The changes in the IR absorption provide information about what chemical bonds are being modified during electron irradiation and chemical enhancement.

**Table 2: Vibrational assignments of polyimide<sup>44-45</sup>**

<b>Assignment (cm<sup>-1</sup>)</b>	<b>Irradiation Absorption (cm<sup>-1</sup>)</b>	<b>Characterization</b>
568	$\delta$ (phenyl)	Phenyl ring deformation
607	$\delta$ (phenyl)	Phenyl ring deformation
636	$\delta$ (C=O)	Carbonyl deformation
705	$\delta$ (C-N-C)	Imide deformation
717	C=O	Carbonyl bending
725	$\delta$ (C-N-C)	Out-of-phase bending of imide ring
734	C=O	Carbonyl bending
752–960	$\delta$ (phenyl)	Phenyl ring deformation
1079	C-O-C stretch	Stretching deformation
1095	$\nu$ (C-N-C)	Imide stretch
1117	$\nu$ (C-N-C)	Imide stretch
1160	C-C	C-C bending
1168	$\nu$ (C-N-C)	Imide stretch
1188	$\delta$ (phenyl)	Phenyl ring deformation
1230	C-N	C-N stretch
1243	$\nu$ (C-O-C)	Bridging C-O-C stretch
1260	$\nu$ (C-O-C)	Bridging C-O-C stretch
1290–1307	$\delta$ (phenyl)	Phenyl ring deformation
1350	C-N	C-N stretch
1376	$\delta$ (C-N-C)	Imide stretch
1390	C-N	C-N stretch
1456–1600	$\nu$ (phenyl)	Phenyl ring C-C stretch
1679–1779	$\nu$ (C=O)	Carbonyl stretch
1825	Cyclic anhydrides, presented in not fully cured polymer	
3020–3155	$\nu$ (C-H)	Phenyl ring C-H stretch
3488	$\nu$ (C-H)	Phenyl ring C-H stretch

## 2.4 Tensile Testing

Tensile testing of polymers can be performed to check the tensile properties of the material. Tensile test methods are used to generate a stress/strain plot to obtain Young's Modulus and strength. Tensile stress,  $\sigma$ , is defined as the applied force,  $F$ , over the original cross-sectional area before loading (Eqn. 12). The cross-sectional area is represented by the yellow area,  $A$ , in **Figure 34**.

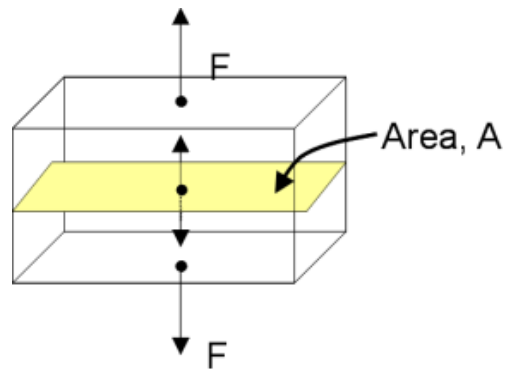


**Figure 34: Tensile stress and cross-sectional area<sup>46</sup>**

$$\sigma = \frac{F}{A} \quad (12)$$

Similarly, tensile strain,  $\epsilon$ , is the relative length of deformation,  $u$ , over the original length of the specimen,  $L$ , that occurs when it is subject to this tensile force. This representation is shown in **Figure 35** below.

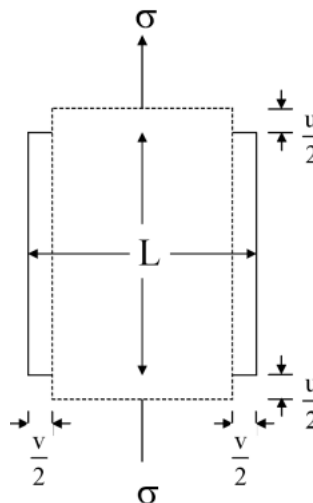


**Figure 35: Tensile strain diagram**<sup>46</sup>

$$\varepsilon = \frac{u}{L} \quad (13)$$

When a tensile force is applied, the specimen elongates in the direction of applied force. As seen in Eqn. 13, the total change divided by the original length equals strain. The applied force also causes a lateral difference, or lateral strain ( $\varepsilon_L$ ). Equation 14, shows the relationship between the width of the sample,  $L_w$ , and the lateral deformation  $v$ .

$$\varepsilon_L = \frac{-v}{L_w} \quad (14)$$

From **Figure 36**, the stress - strain plot provides the proportional point, or proportional limit A, where the amount of stress is proportional to strain, otherwise known as Hooke's Law. This linear region slope corresponds to the material's Young's modulus (E). Point B is the yield point or yield stress typically represented as  $\sigma_y$ . This is not to be confused with the secondary electron yield ( $\sigma_{\text{yield}}$ ) used previously in section 2.3. This point represents the transition from elastic to plastic region, or the maximum force the material can withstand elastically. Point C is called the lower yield point. At this stage, the material continues to elongate while the stress decreases. Point D is known as the ultimate tensile strength point. This is the highest point in the stress/strain plot and represents the total maximum load the material can withstand while being stretched or pulled. Lastly, the material will become weaker up to the fracture point E.

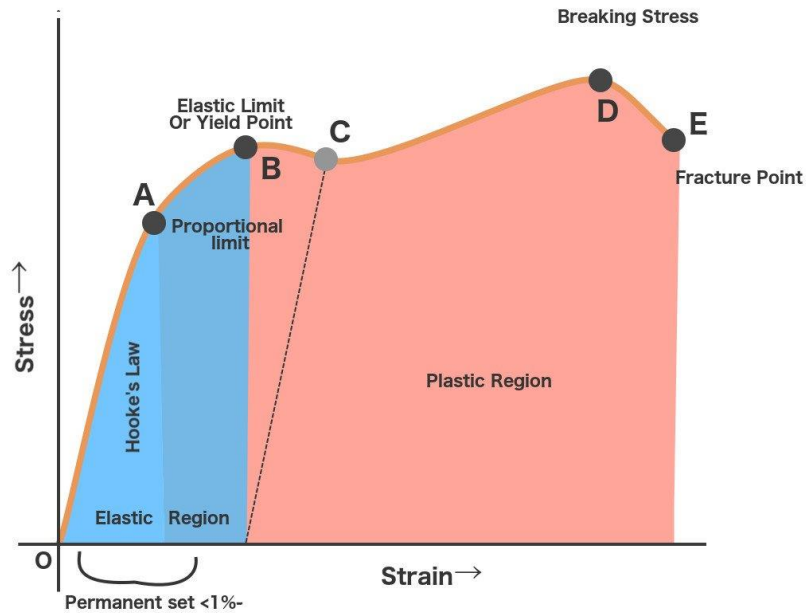


**Figure 36: Stress & Strain diagram<sup>47</sup>**

Mechanical testing of the samples was conducted using a Dynamic Mechanical Analysis (DMA) Q800 – TA instruments. The DMA machine has several modes of deformation specific to the sample or desired characterization. For this study, the device was operated under the displacement-controlled mode and utilized a film tension clamp. The sample was placed in between a fixed and a moveable clamp while applying a controlled displacement as shown in **Figure 37: Tension clamp experimental setup<sup>48</sup>**.



**Figure 37: Tension clamp experimental setup<sup>48</sup>**

The method of testing was used to create a stress - strain curve. There was a preload of 0.01 N and an initial displacement of 1.0  $\mu\text{m}$ . A displacement ramp of 100  $\mu\text{m}$  per minute took place

until the sample reached 1000  $\mu\text{m}$ . It took a total of 10 minutes to reach the maximum displacement after the ramping began. This method employs the ASTM standard D638 – 14.

The sample size was constructed by back solving for the required area based on the DMA's maximum allowable force and a yield stress value of 69 MPa. This yield stress corresponded to DuPont's yield point at 3% elongation. Their values were recorded at 23°C (73°F) compared to an average of 27°C (80°F) for this study. The values are used for comparison and understanding of experimental calculations used in this study. Using Eqn. 12, the calculations are as follows,

$$\sigma = \frac{F}{A}$$

$$69 \times 10^6 \text{ Pa} = \frac{18 \text{ N}}{A}$$

$$A = 2.60869 \times 10^{-7} \text{ m}^2 = 2.60869 \times 10^{-3} \text{ cm}^2$$

The three-mil thickness (0.00762 cm) Kapton samples were constant for every test. Therefore, the cross-sectional area is the thickness times the width of the sample.

$$A = 0.00762 * \text{Width} = 2.60869 \times 10^{-3} \text{ cm}^2$$

$$\text{Width} = 0.10225 \text{ cm}$$

In order to witness the region past the yield point of the samples, the width of each specimen was cut under 0.10225 cm.

### Chapter 3: Results and Discussion

Characterization of the PI films began immediately after the samples were removed from the irradiation vacuum chamber (Jumbo). First, irradiated Kapton samples were visually inspected after breaking the vacuum and the healing process began.

Homogeneous irradiation of PI samples with high-energy electrons depends on the mounting and position of the sample. **Figure 38** below shows several different PI films immediately after breaking vacuum post-irradiation. It can clearly be seen that the bottom part of the film received a far higher electron dose than the rest of the coupon. Due to this inhomogeneous dose, these samples were not used for this study and a larger sample size was used to ensure that the larger area of the sample received a homogeneous electron dose.

It should be noted that electron-damaged films began to heal, i.e. recover its optical properties towards the pristine film, immediately after they are exposed to air, as can be seen in each figure. However, if the irradiation dose is high enough, the healing process is incomplete and results in permanent damage as shown in all figures. All characterizations were performed on samples that had been exposed to the atmosphere for at least 6 days after irradiation. The recovery process took place during the first two days, and after that further material, healing was not visually evident. We interpreted this as evidence that the material properties had stabilized. In all cases, measurements were performed on the pristine, electron irradiated, and chemically treated samples on the same day in order to minimize variability between experimental conditions.

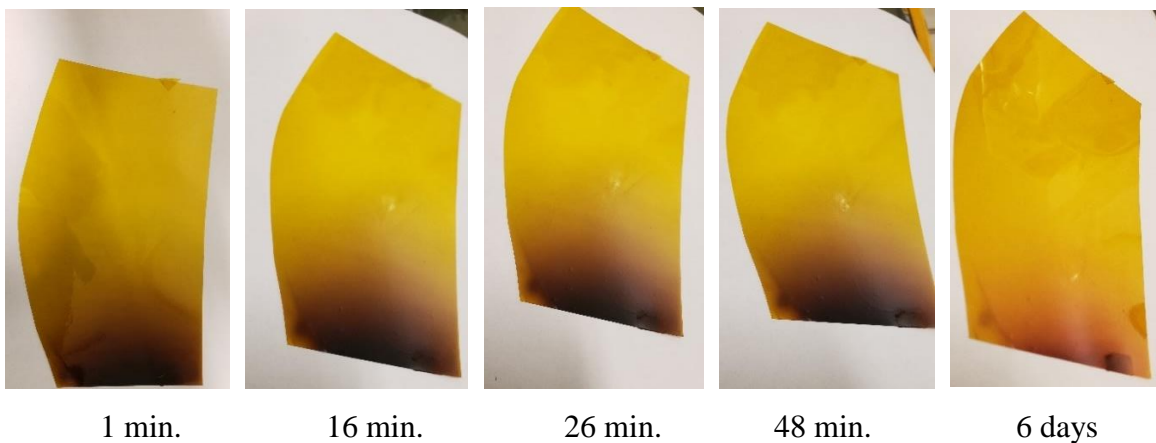


**Figure 38: Non-homogenous electron aged sample. Time of post-irradiation atmospheric exposure is indicated below each panel.**

**Figure 39** has multiple images that were taken at random time intervals to show the healing process of the irradiated PI material after its exposure to air. The far-left hand image shows the specific orientation the film was mounted on the rotating aluminum carousel to ensure a homogeneous electron dose received by the samples. Visual inspection of these samples reveals the uniform discoloration of the material after high energy electron bombardment, so they were utilized as the electron aged samples for experimentation.

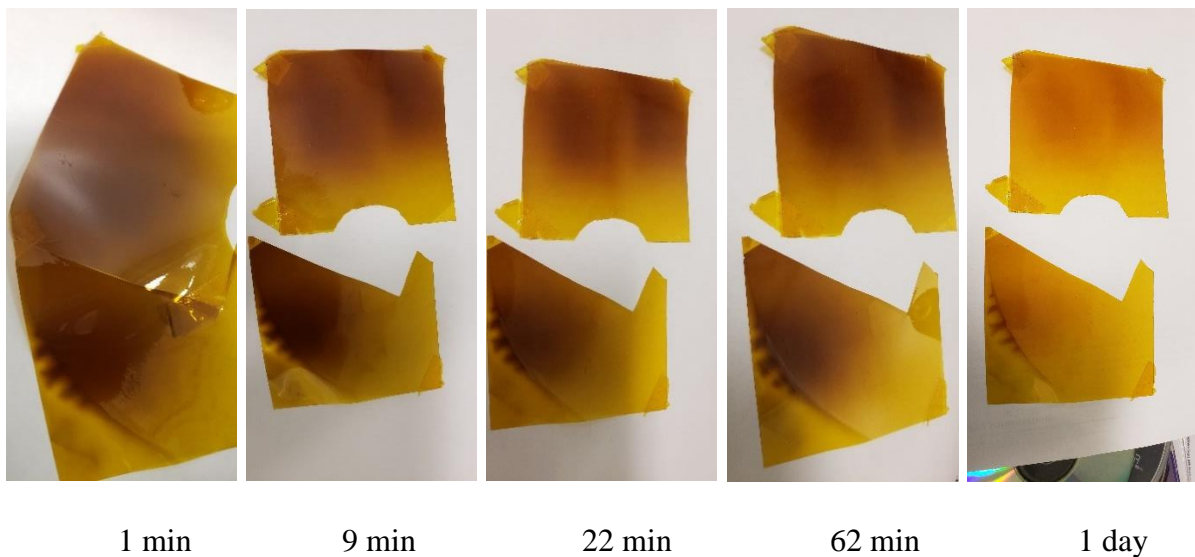


**Figure 39: Electron aged sample healing process. Time of post-irradiation atmospheric exposure is indicated below each panel.**

Air-induced healing process of the fluorinated PI material is represented in **Figure 40**. During the irradiation process, this sample covered half of the aluminum carousel, as discussed in chapter 4 **Figure 16**. Comparison of the healing process of electron-damaged and fluorinated PI films showed that the latter did not change its transmission characteristics significantly after ~ 1 hour of air exposure, suggesting more stability compared with the irradiated but non-fluorinated samples.

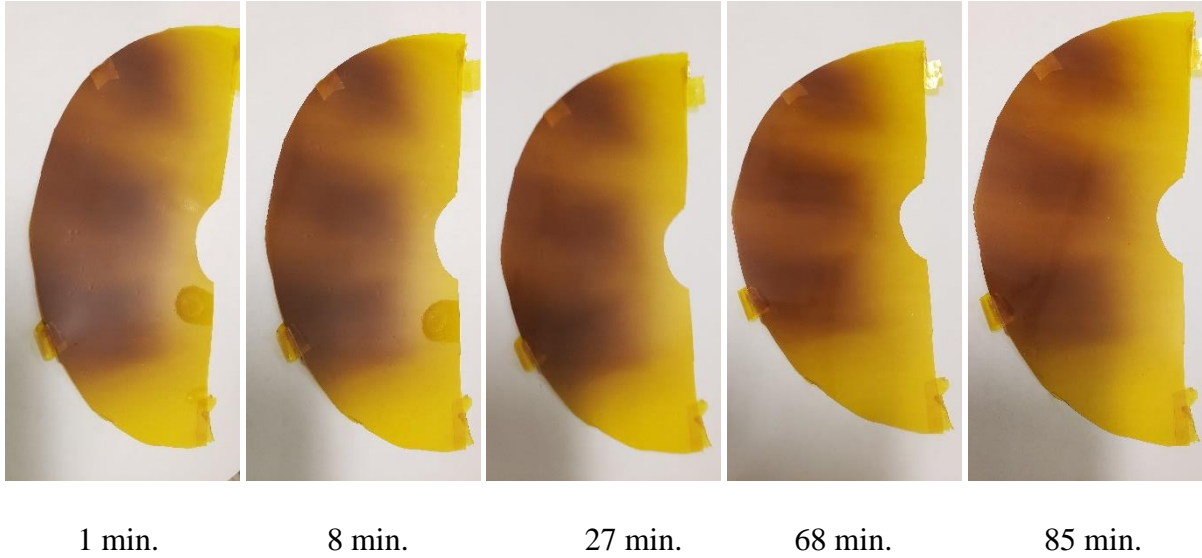


**Figure 40: Fluorinated sample healing process. Time of post-irradiation atmospheric exposure is indicated below each panel.**

### 3.1 Electrical Conductivity Results

Volume resistivity measurements were conducted using six experimental test voltages ranging from 50 to 1000 V. Each experimental set was conducted twice for each of the three films in this study. The first set of experiments are shown in **Table 3**,

**Table 4**, and **Table 5**.

**Table 3: Pristine sample; First experimental electrical conductivity measurements**

<b>Pristine Sample: Experimental Set 1</b>			
<b>Current (A)</b>	<b>Voltage (V)</b>	<b>Volume Resistivity (<math>\Omega\cdot\text{cm}</math>)</b>	<b>Conductivity (<math>1/\Omega\cdot\text{cm}</math>)</b>
2.46E-12	50	6.12E+16	1.63E-17
1.48E-12	100	2.03E+17	4.92E-18
3.98E-12	250	1.89E+17	5.29E-18
3.43E-13	500	4.38E+18	2.28E-19
1.65E-11	750	1.36E+17	7.33E-18
1.92E-11	1000	1.56E+17	6.40E-18
<b>Average Conductivity</b>			6.57E-18

**Table 4: Aged sample; First experimental electrical conductivity measurements**

<b>Aged Sample: Experimental Set 1</b>			
<b>Current (A)</b>	<b>Voltage (V)</b>	<b>Volume Resistivity (<math>\Omega\cdot\text{cm}</math>)</b>	<b>Conductivity (<math>1/\Omega\cdot\text{cm}</math>)</b>
5.60E-12	50	2.68E+16	3.72581E-17
7.26E-12	100	4.14E+16	2.41547E-17
2.26E-12	250	3.33E+17	3.00221E-18
1.33E-11	500	1.13E+17	8.8565E-18
2.89E-11	750	7.81E+16	1.28122E-17
1.70E-11	1000	1.77E+17	5.66409E-18
<b>Average Conductivity</b>			1.53E-17

**Table 5: Fluorinated sample; First experimental electrical conductivity measurements**

<b>Fluorinated Sample: Experimental Set 1</b>			
<b>Current (A)</b>	<b>Voltage (V)</b>	<b>Volume Resistivity (<math>\Omega\cdot\text{cm}</math>)</b>	<b>Conductivity (<math>1/\Omega\cdot\text{cm}</math>)</b>
5.86E-13	50	2.57E+17	3.90E-18
6.43E-13	100	4.68E+17	2.14E-18
4.32E-12	250	1.74E+17	5.76E-18
1.36E-11	500	1.11E+17	9.04E-18
9.35E-12	750	2.41E+17	4.15E-18
2.11E-11	1000	1.42E+17	7.03E-18
<b>Average Conductivity</b>			5.33E-18

**Table 6, Table 7, and Table 8** represent the second set of results.

**Table 6: Pristine sample; Second experimental electrical conductivity measurements**

<b>Pristine Sample: Experimental Set 2</b>			
<b>Current (A)</b>	<b>Voltage (V)</b>	<b>Volume Resistivity (<math>\Omega\cdot\text{cm}</math>)</b>	<b>Conductivity (<math>1/\Omega\cdot\text{cm}</math>)</b>
2.65E-12	50	5.66772E+16	1.76E-17
2.26E-12	100	1.33029E+17	7.52E-18
5.52E-12	250	1.36147E+17	7.35E-18
7.17E-12	500	2.09562E+17	4.77E-18
1.64E-11	750	1.37126E+17	7.29E-18
5.14E-11	1000	5.84588E+16	1.71E-17
<b>Average Conductivity</b>			1.03E-17

**Table 7: Aged sample; Second experimental electrical conductivity measurements**

<b>Aged Sample: Experimental Set 2</b>			
<b>Current (A)</b>	<b>Voltage (V)</b>	<b>Volume Resistivity (<math>\Omega\cdot\text{cm}</math>)</b>	<b>Conductivity (<math>1/\Omega\cdot\text{cm}</math>)</b>
6.54E-13	50	2.30E+17	4.35E-18
1.61E-12	100	1.87E+17	5.35E-18
4.36E-12	250	1.72E+17	5.80E-18
8.06E-12	500	1.86E+17	5.37E-18
1.54E-11	750	1.47E+17	6.81E-18
5.43E-11	1000	5.53E+16	1.81E-17
<b>Average Conductivity</b>			7.63E-18

**Table 8: Fluorinated sample; Second experimental electrical conductivity measurements**

<b>Fluorinated Sample: Experimental Set 2</b>			
<b>Current (A)</b>	<b>Voltage (V)</b>	<b>Volume Resistivity (<math>\Omega\cdot\text{cm}</math>)</b>	<b>Conductivity (<math>1/\Omega\cdot\text{cm}</math>)</b>
5.57E-14	50	2.70E+18	3.71E-19
1.25E-12	100	2.41E+17	4.15E-18
3.71E-12	250	2.02E+17	4.94E-18
5.10E-12	500	2.95E+17	3.39E-18
1.98E-11	750	1.14E+17	8.80E-18
5.54E-11	1000	5.43E+16	1.84E-17
<b>Average Conductivity</b>			6.68E-18

The experimental error bars are shown in **Figure 41** below.

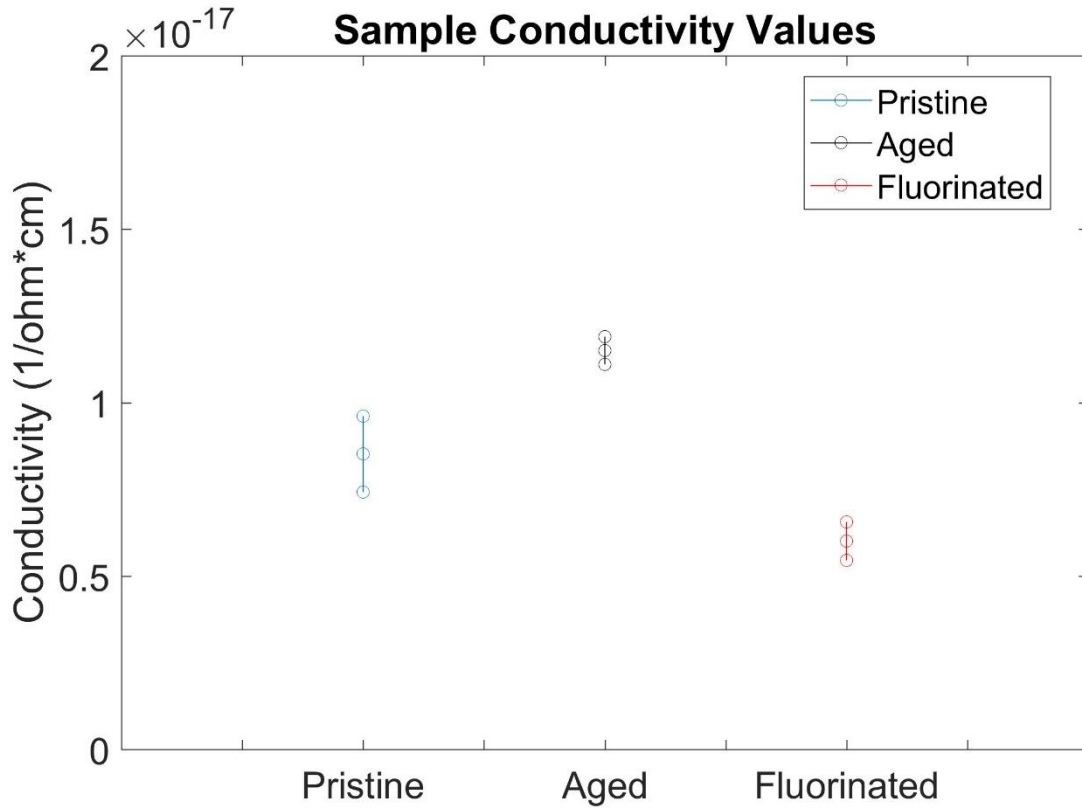


**Figure 41: Electrical conductivity error bars**

The first set of experimental runs suggested that the conductivity values increased after the electron irradiation and decreased after the fluorination. The current readings were extremely small and close to the lower end of the instrumentations' operating range. Additionally, the initial ground level current readings changed with every tested sample after storing the previous test charge. Statistical error bars were extremely close to all values for all three films suggesting there may or may not have been a permanent change. Similar findings were recorded for a second set of experimental runs and error approximation. The measurements were outside the bounds of experimental uncertainty, and therefore, we cannot conclude that the irradiation changed the conductivity.

As discussed in Section 2.3, the conductivity measurements based on ASTM standard may not be a suitable technique for the charge transport properties assessment of the irradiated PI. The ASTM method measures the current passing through the material under an applied electric field. The material being measured is macroscopic in scale and contains many different “pathways” that electrons can travel between the two plates. This methodology measures the bulk resistivity of the most conductive pathways in the material. In the case of highly resistive materials, the measurement results are significantly dependent on the sample handling technique, presence of external contaminants (such as water), among other factors. This explains large errors in the measurements on pristine, irradiated, and fluorinated samples.

The SPD method, on the other hand, injects electrons into the material and measures the loss of these electrons to the grounded plate at the back of the material. Therefore, electrons implanted into a more resistive domain take longer to dissipate, as their pathway is less conductive. This methodology measures a bulk resistivity that is limited by the least conductive pathways in the material. In other words, the effect of the external random contaminants presented in ASTM measurements is significantly suppressed during SPD measurements. Sadly, the proper assessment of the PI samples charge transport was not possible during this study due to the major renovation of the experimental facilities.

For the sample constituent of only Kapton matrix, the results returned by the ASTM and SPD methods are expected to be very similar. However, since conductivity was evaluated after recovery of irradiation damage, it is most likely beyond or on the borderline of the apparatus detection limit. Addition of the fluoride into the polymer matrix should change the

charge transport properties of the PI material, but this change must be still subtle and not detected by the ASTM- based technique.

### 3.2 FTIR Spectroscopy Results

Vibrational spectroscopy was performed on all samples using a Nicolet 6700 FTIR spectrometer. Each spectrum is recorded within the instrumentation's reflection mode in 400 to 4000  $\text{cm}^{-1}$  range. FTIR absorption spectra for the pristine, electron-irradiated (aged), and fluorinated samples are presented in **Figure 42**, **Figure 43**, and **Figure 44**.

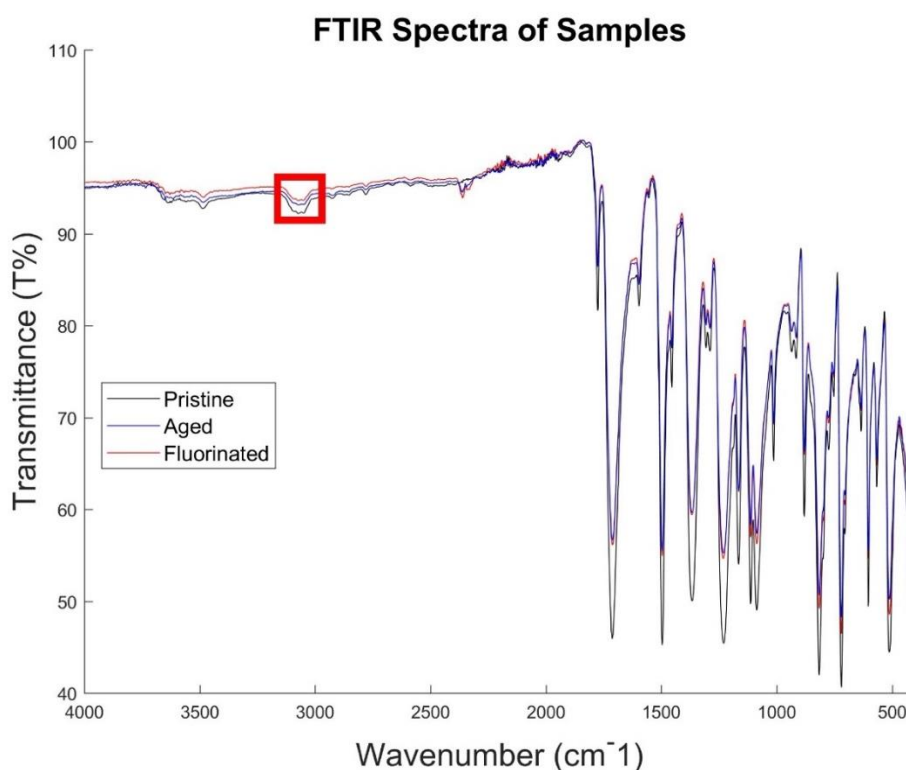


**Figure 42: FTIR spectra of pristine, electron aged, and fluorinated samples**

For proper comparison of measured spectra, a common baseline was generated and subtracted from each spectrum to distinguish between the relative intensities of the samples. Table 2 was used to identify some of the characteristic vibrational assignments within the experimental spectra. The functional group utilized to normalize the spectra was phenyl ring C-H stretch. The phenyl ring C-H stretching band located at 3020 to 3155  $\text{cm}^{-1}$ , is shown by the red box in **Figure 42** above. This phenyl peak was the most obvious in the functional group region that did not have significant differences influenced by changes in intensity or

simply instrumental error. **Figure 43** shows a closer view of what points were used to normalize the spectra. The pristine and fluorinated spectra were shifted up or down to meet the aged samples' spectrum in the middle. Equations 15 and 16 represent how the coordinate points were used to multiple a constant to the spectrum.

$$\text{Normalization1} = \text{Pristine spectrum} * \left(\frac{93.18}{92.25}\right) \quad (15)$$

$$\text{Normalization2} = \text{Fluorinated spectrum} * \left(\frac{93.18}{93.63}\right) \quad (16)$$

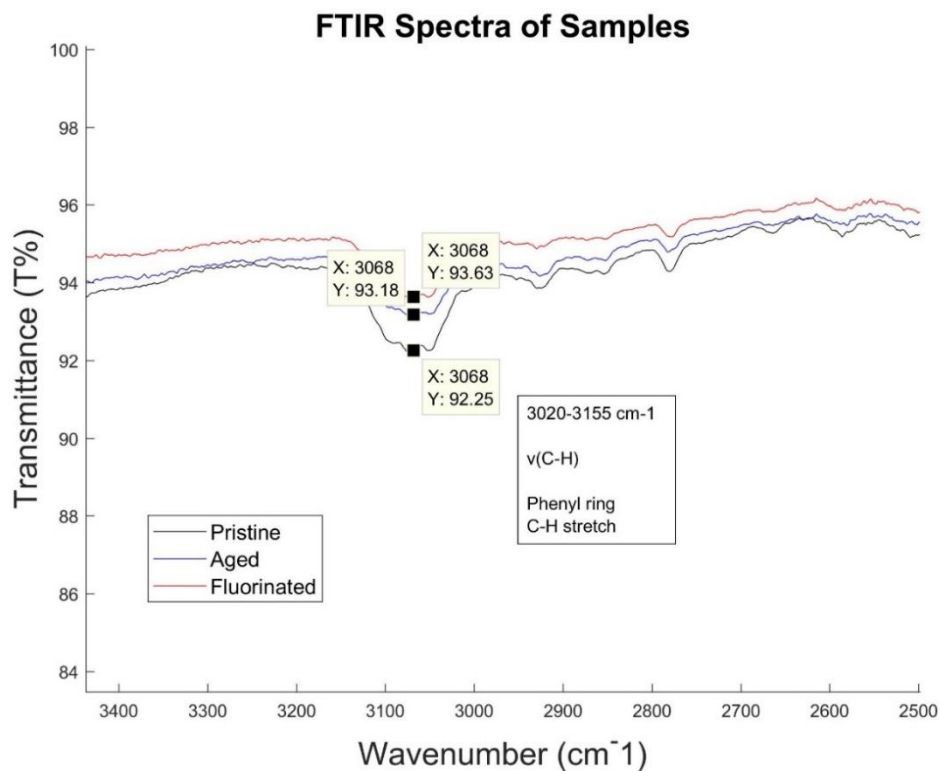


**Figure 43: Normalization at the phenyl absorption peak**

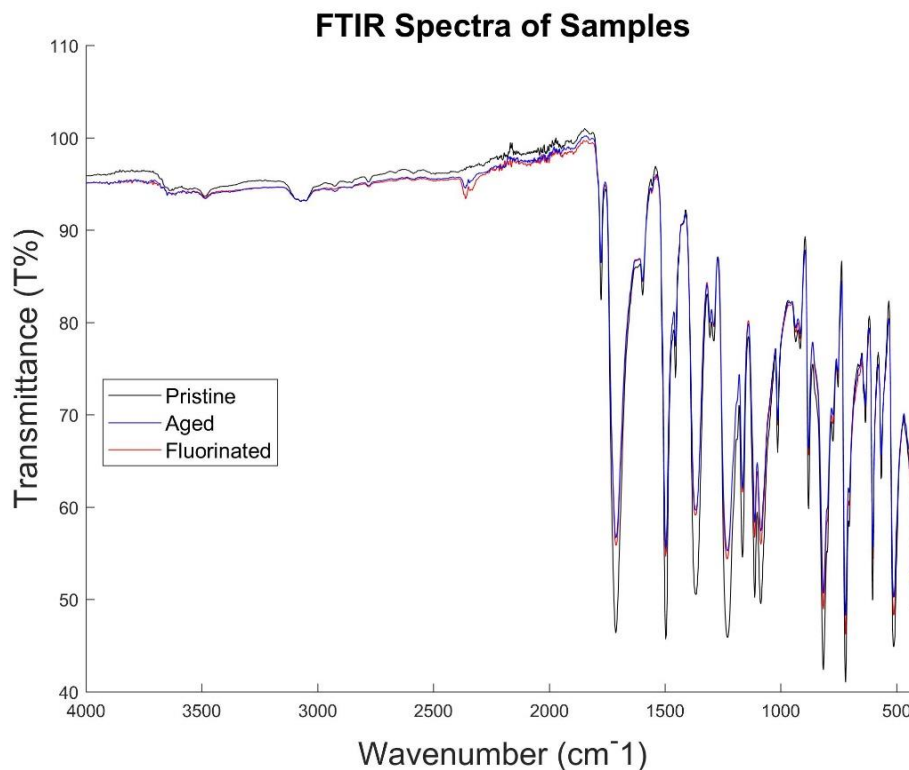


**Figure 44: Normalized FTIR spectra of pristine, electron aged, and fluorinated samples**

The films' absorption spectra distinguished a difference between the pristine and both the aged and fluorinated samples. In the electron irradiated and fluorinated samples, a new absorption band developed, which corresponds to the absorption band of the asymmetric stretch of CO<sub>2</sub>.<sup>49</sup> Earlier studies have indicated that electron irradiation leads to the formation of evolved gases from Kapton previously seen in **Figure 10**.<sup>25</sup> These gases reported to evolve from Kapton during irradiation include CO<sub>2</sub>, which is identifiable as a doublet peak in the aged and fluorinated sample spectra at 2400 to 2300 cm<sup>-1</sup>. This new peak formation and relative intensity can be seen in **Figure 45** below.

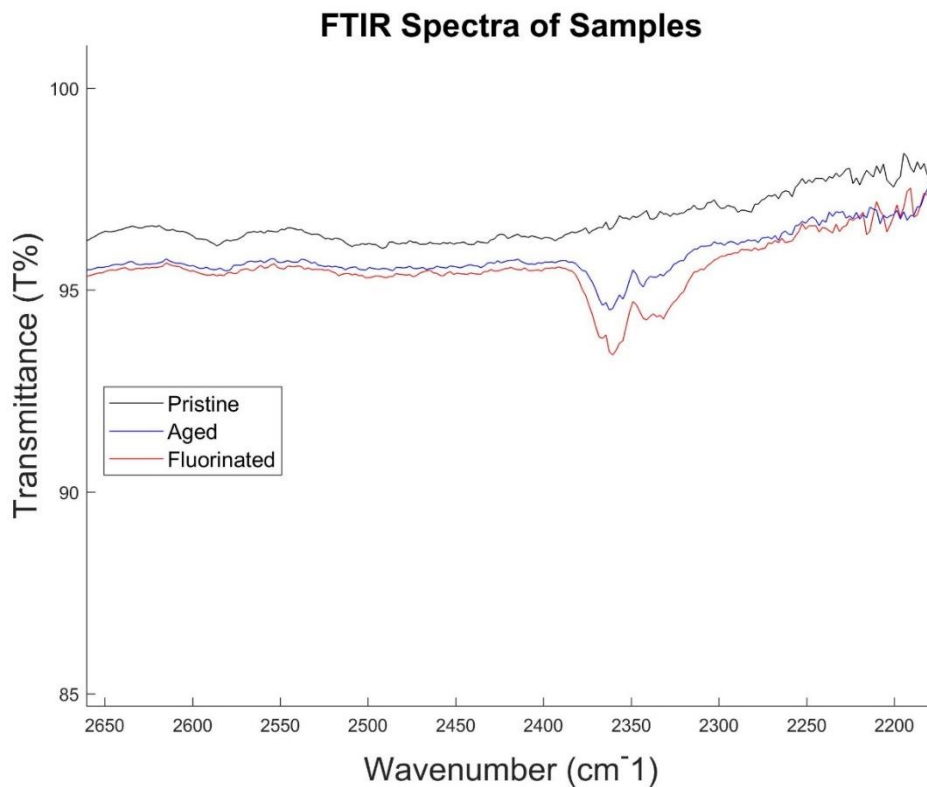


**Figure 45: Close-up of the CO<sub>2</sub> doublet peak**

As a reference, the CO<sub>2</sub> spectra was retrieved from the National Institute of Standards and Technology (NIST) Standard Reference Database 69: *NIST Chemistry WebBook*. The spectrum was collected and measured from dispersive instruments using carefully selected solvents. Therefore, measurements on FTIR instrumentation in different chemical environments differ in detail. The spectrum can be seen in **Figure 46** below. The CO<sub>2</sub> doublet peak, asymmetric stretch, is clearly visible between ~2300 and 2500 cm<sup>-1</sup>.

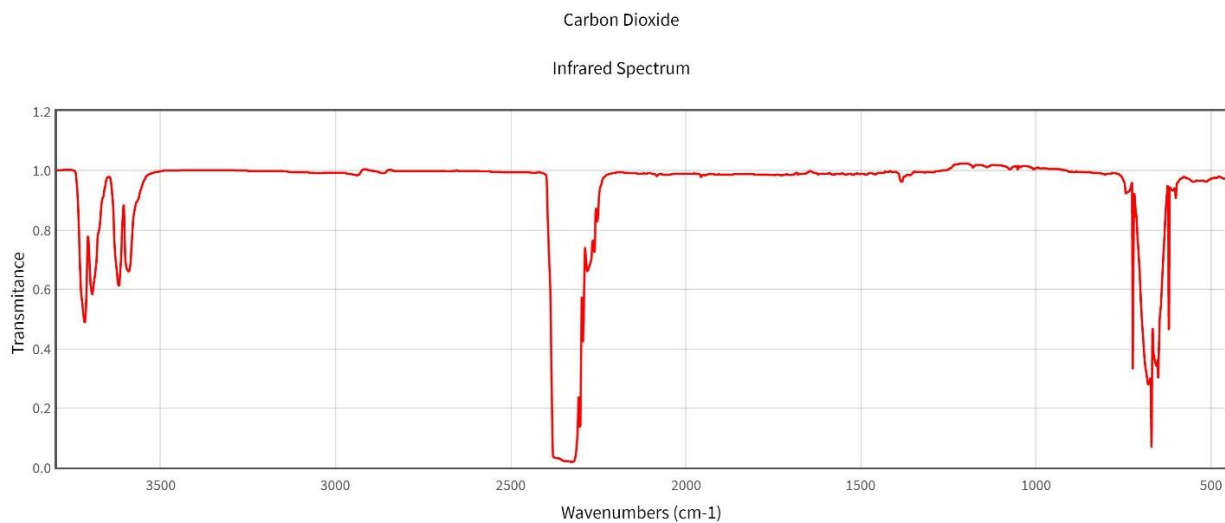


**Figure 46: FTIR spectrum of CO<sub>2</sub>**<sup>50</sup>

Furthermore, when comparing both samples to the pristine films' absorption spectra, the overall intensity changed depending on the regime. The overall intensity decreased between  $\sim 1780$  and  $500\text{ cm}^{-1}$  and increased between  $4000$  and  $\sim 1780\text{ cm}^{-1}$ . This effect has been seen in studies of ion bombardment of Kapton.<sup>43</sup> The small peaks at  $2780$ ,  $2860$ , and  $2930\text{ cm}^{-1}$  were not experimentally reproducible and grew/shrank on all samples from measurement to measurement, as seen in **Figure 47** below. We attribute these peaks to adsorbed gases on the PI films, largely, CO<sub>2</sub>.

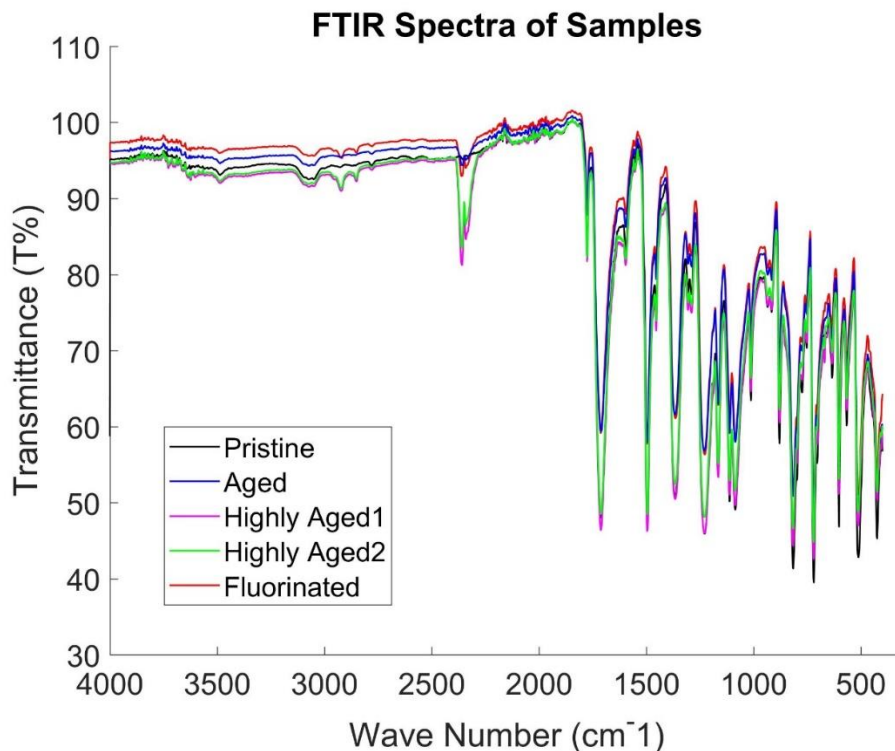


**Figure 47: FTIR spectra of all experimental samples in addition to two highly electron irradiated PI films**

The above figure displays the FTIR absorption spectra for the pristine, electron aged, and fluorinated PI samples in addition to two other samples. The PI samples were electron aged with an unknown electron irradiation time and were used to supplement the findings. In the legend of **Figure 47**, they are named Highly Aged1 and Highly Aged2. The samples were extremely brittle and much darker than the PI samples used in this study. The highly irradiated samples are proportional to the larger CO<sub>2</sub> peak intensity. This relationship does not aim to contrast the exact dose versus the relative peak height, but rather it does correlate the effect of electron irradiation PI on its chemical functional groups.

In summary, FTIR measurements of the electron irradiated and fluorinated samples revealed a formation of a new absorption band corresponding to the asymmetric stretch of CO<sub>2</sub>. The CO<sub>2</sub> doublet peak is clearly visible between ~2300 and 2500 cm<sup>-1</sup> in FTIR spectra of both irradiated and fluorinated samples. The doublet discovery is supported by the findings in measurements of gas evolved from polymers during electron irradiation.<sup>25</sup> The amount of CO<sub>2</sub> evolved versus radiation dose is quantitatively represented in **Figure 10**. Additionally, the

intensity of the doublet increased with an increase in electron dosage. The two highly irradiated samples with permanent embrittlement (not flexible and easily broken under moderate bending by hand) were visibly darker than the pristine Kapton. This suggests that they were irradiated with a higher fluence of electrons. Similarly, the previous study correlates an increase of the overall evolved CO<sub>2</sub> to an increase in electron dose.

### 3.2 Tensile Properties

**Table 9** summarizes the mechanical properties for the pristine, electron aged, and fluorinated samples. The results suggest an increase in both the modulus and yield stress for the irradiated samples.

**Table 9: Mechanical properties of pristine, aged, and fluorinated Kapton**

Test Method	Mechanical Property	Pristine	Electron Aged	Fluorinated
Displacement Controlled	Tensile Modulus, E (GPa)	2.12	2.40	2.67
	Yield Stress at 0.2% elongation, (MPa)	27.15	37.98	32.93

The 0.2% offset line parallel to the linear region crosses the curve at the yield stress point above the proportional limit, as shown in Figure 48. The calculations followed the ASTM E111 – 17.

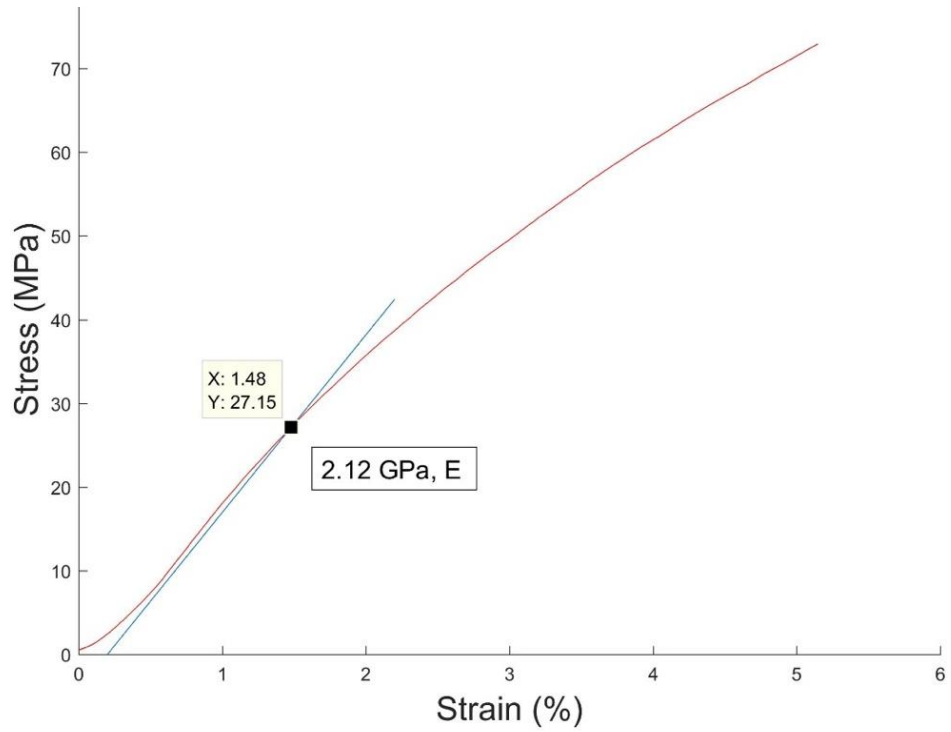


**Figure 48: Stress versus strain graph of the Pristine sample**

**Figure 49** shows representative superimposed stress-strain graphs for all three experimental samples. The increase of Young's modulus (tensile modulus) was observed for the electron-damaged PI samples.

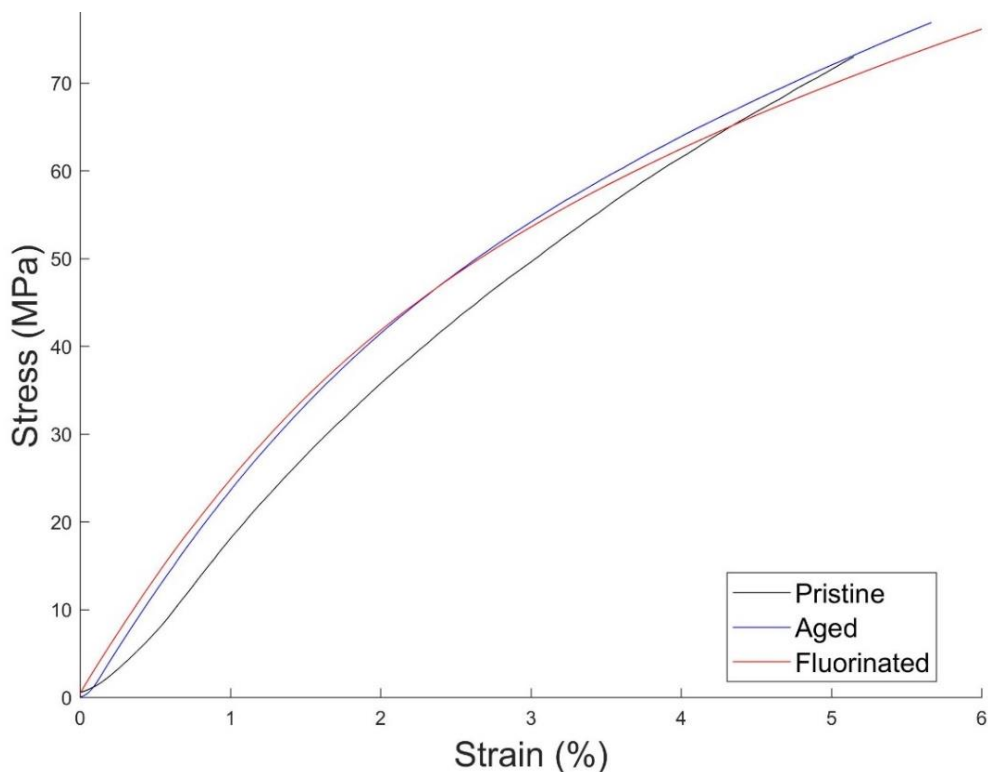


**Figure 49: Representative stress - strain graphs**

The tensile modulus increased for the electron-aged and fluorinated samples. This is indicative of increased cross-linking due to the material irradiation, which manifests itself as increased embrittlement of the samples. This finding is supported by the ReaxFF calculations employed to simulate the effects of electron bombardment on the PI structure, which have been reported in earlier publications.<sup>28</sup> The results of these simulations indicate chemical damage localized in the imidic rings and ether linkages, leading to increased cross-linking and chain scission.

In summary, bulk conductivity values deduced from the ASTM-based measurements demonstrated the increase after the electron age and decrease after the fluorination. However, these results may be not conclusive because the conductivity measurements did not show any change in conductivity that was outside the bounds of experimental uncertainty. Although several studies have shown long-term increases in dark conductivity, the fact that these polymers were allowed to heal fully in the atmosphere could be the reason that no change was detected. The experimental setup was also at the limit of its sensitivity, which led to higher uncertainties, further obscuring the data.

Generally, electron irradiation of the PI sample causes increased conductivity as a result of the PI's intermolecular bonds breaking. The formation of unpaired electrons in the damaged material occur after the high-energy electron irradiation. The rupture of the radicals leads to cross-linking and formation of a larger pi-bonded carbon network in the PI.<sup>11</sup> Ether breakage in the material occurs after the irradiation forming a metastable carbonyl. In addition, the damage caused by the electron bombardment increases the trap states in the material's bandgap. As a result, there is an increase in electrical conductivity in the material, otherwise named from the previous study as dark conductivity.

## Chapter 4: Conclusions and Future Work

The development of novel engineered materials, including the exposure of PI to high energy ionizing irradiation, is an actively evolving engineering field where the efforts of many researchers are focused. Generally, ionizing radiation is widely used for the development of advanced polymeric materials for a broad range of industries, including the production of insulating, heat-shrink, and shape-memory materials.<sup>51-53</sup>

Fluorination of the electron-modified PI has a lot of potential for the realization of the material with higher optical transparency and lower dielectric constants, especially important for the mitigation of the ESD effects on the spacecraft. Ultimately, flooding the chamber with Trifluoromethane after electron irradiation did not change the mechanical and electrical properties of the PI. Although the effects of fluorination on this electron irradiated PI were unsuccessful, the effects of electron-induced damage on the material were successfully characterized. The reactive state of electron-irradiated PI has been proven to react, or heal, under exposure to partial pressures of oxygen and water vapor.<sup>11</sup> This suggests chemical modification with a gas of choice is possible as already seen when the material is exposed to air.

The electrical bulk conductivity values were indeterminate. The results did not distinguish significant differences between conductivity measurements for either sample. The statistical error bars were extremely close to all the conductivity values. Many measurements were outside the bounds of experimental uncertainty, making it impossible to conclude if the irradiation resulted in a change in the conductivity. In future studies, charge transport measurements on the irradiated and fluorinated samples will be repeated using more suitable SPD technique, which was unavailable during the time of the study.

FTIR measurements showed significant differences and clear evidence of a new absorption peak. The overall intensity of the aged and fluorinated sample decreased between  $\sim 1780$  and  $500\text{ cm}^{-1}$  and increased between  $4000$  and  $\sim 1780\text{ cm}^{-1}$  as seen in the ion-induced damaged PI films.<sup>43</sup> A new doublet peak emerged in the aged and fluorinated sample spectra at  $2400$  to  $2300\text{ cm}^{-1}$ . The future work related to this study will further inspect small peaks located at  $2780$ ,  $2860$ , and  $2930\text{ cm}^{-1}$  which were not experimentally reproducible as they grew or shrunk on all samples from measurement to measurement. Additionally, future work will

pursue the FTIR absorption spectra of electron-irradiated PI film before exposing it to the atmosphere. This will be representative of the actual material on a spacecraft while on orbit.

Tensile measurements showed higher modulus values for the electron irradiated samples, indicating crosslinking and chain scission. There was no direct correlation between the yield stress values of the PI samples; further mechanical tests may allow for a statistical representation of the values. The findings were supportive of the molecular dynamics simulations that involved an electron irradiated sample of Kapton.

The research presented here provided an understanding of the possibilities of chemical modification of Kapton after electron irradiation. Although it provided a valid method for initiation of desired chemical changes, the chemical used (Trifluoromethane) did not impact the material properties as expected. However, by exposing the reactive PI film to the atmosphere, a chemical modification, known as material healing, changed the material properties. The magnitude of the change is dependent on the electron dose, or extent of the material aging. Future work will aim towards investigating a new reactant to modify the material when it is in its post-irradiation reactive state in a way that tailors its physical properties depending on the application.

## References

<sup>1</sup>Sato, N.; Suzuki, K.; Chiba, U.; Miyake, H.; Tanaka, Y.; Okumura, T.; Kawakita, S.; Takahashi, M.; Koga, K. Photoelectron Emission on Polyimide Films Irradiated by Proton. In Proceedings of the IEEE 2018 Condition Monitoring and Diagnosis (CMD), Perth, WA, Australia, 23–26 September 2018; pp. 1–4, doi:10.1109/CMD.2018.8535625.

<sup>2</sup>Arnaout, M.; Paulmier, T.; Dirassen, B.; Payan, D. Study of radiation induced conductivity and photoconduction phenomenon for materials used in space environment. *J. Electrostat.* **2016**, *84*, 48–53, doi:10.1016/j.elstat.2016.09.001.

<sup>3</sup>Wu, J.; Miyahara, A.; Khan, A.; Iwata, M.; Toyoda, K.; Cho, M.; Zheng, X. Effects of energetic electron and proton irradiation on electron emission yield of polyimide induced by electron and photon. *Trans. Jpn. Soc. Aeronaut. Space Sci.* **2014**, *12*, 13–19, doi:10.2322/tastj.12.Pr\_13.

<sup>4</sup>G. P. Ginet, T. P. O'Brien, S. L. Huston, W. R. Johnston, T. B. Guild, R. Friedel, C. D. Lindstrom, C. J. Roth, P. Whelan, R. A. Quinn, D. Madden, S. Morley, and YiJiun Su., "AE9, AP9 and SPM: New Models for Specifying the Trapped Energetic Particle and Space Plasma Environment," *Space Science Reviews*, vol. 179, pp. 579-615, 2013/11/01 2013.

<sup>5</sup>O'Brien, T.P.; Johnston, W.R.; Huston, S.L.; Roth, C.J.; Guild, T.B.; Su, Y.J.; Quinn, R.A. Changes in AE9/AP9-IRENE Version 1.5. *IEEE Trans. Nucl. Sci.* 2018, *65*, 462–466.

<sup>6</sup>Sharon Bewick, Richard Parsons, Therese Forsythe, Shonna Robinson, and Jean Dupon, "4.4: The Properties of Protons, Neutrons, and Electrons"

[https://chem.libretexts.org/Courses/Eastern\\_Wyoming\\_College/EWC%3A\\_Introductory\\_Chemistry\\_\(Budhi\)/04%3A\\_Atoms\\_and\\_Elements/4.4%3A\\_The\\_Properties\\_of\\_Protons%2C\\_Neutrons%2C\\_and\\_Electrons](https://chem.libretexts.org/Courses/Eastern_Wyoming_College/EWC%3A_Introductory_Chemistry_(Budhi)/04%3A_Atoms_and_Elements/4.4%3A_The_Properties_of_Protons%2C_Neutrons%2C_and_Electrons)

<sup>7</sup>Marletta, G.; Iacona, F. Heat-induced versus particle-beam-induced chemistry in polyimide. *Nucl. Instrum. Methods Phys. Res. B* **1993**, *80*, 1045–1049, doi:10.1016/0168-583X(93)90733-M.

<sup>8</sup>Marletta, G. Chemical reactions and physical property modifications induced by keV ion beams in polymers. *Nucl. Instrum. Methods Phys. Res. B* **1990**, *46*, 295–305, doi:10.1016/0168-583X(90)90716-8.

<sup>9</sup>Bolt, R.O.; Garrol, J.G. *Radiation Effects on Organic Materials*; Academic: New York, NY, USA, 1963.

<sup>10</sup>Bovey, F.A. *The Effect of Ionizing Radiation on Natural and Synthetic High Polymers*; Interscience: New York, NY, USA, 1958.

<sup>11</sup>Elena A. Plis, Daniel P. Engelhart, Russell Cooper, Dale D. C. Ferguson, & Ryan Hoffmann. (2018). Effect of environment on charge transport properties of polyimide films damaged by high-energy electron radiation. *Journal of Vacuum Science & Technology: Part B-Nanotechnology & Microelectronics*, 36(5), N.PAG. <https://doi-org.libproxy.unm.edu/10.1116/1.5044184>

<sup>12</sup>A. Tyutnev, V. Saenko, E. D. Pozhidaev, and R. Sh. Ikhsanov, *IEEE Trans. Plasma Sci.* **43**, 2915 (2015).

<sup>13</sup> T. Goorley, "MCNP6.1.1-Beta Release Notes", LA-UR-14-24680 (2014).

<sup>14</sup>M. J. Berger, J. S. Coursey, M. A. Zucker, and J. Chang, ESTAR, PSTAR, and ASTAR: Computer Programs for Calculating Stopping-Power and Range Tables for Electrons, Protons, and Helium Ions (version 1.2.1). Available at: <http://physics.nist.gov/Star>. National Institute of Standards and Technology, Gaithersburg, MD (1999)

<sup>15</sup>Plis, E., Engelhart, D. P., Barton, D., Cooper, R., Ferguson, D., & Hoffmann, R. (2017). Degradation of polyimide under exposure to 90keV electrons. *Physica Status Solidi b - Basic Solid State Physics*, (7). <https://doi-org.libproxy.unm.edu/10.1002/pssb.201600819>

<sup>16</sup>J. Brunson, "Hopping conductivity and charge transport in low density polyethylene," Ph.D. dissertation (Utah State University, 2010).

<sup>17</sup>Y. N. Gartstein and E. M. Conwell, *Phys. Rev. B* 51, 6947 (1995).

<sup>18</sup>S. Noro and T. Yamadaya, *J. Polym. Sci.* 29, 359 (1991).

<sup>19</sup>S. R. Kumbhani, T. S. Cline, M. C. Killian, J. M. Clark, W. J. Keeton, L. D. Hansen, R. B. Shirts, D. J. Robichaud, and J. C. Hansen, *Int. J. Chem. Kinet.* 47, 395 (2015).

<sup>20</sup>J. Lee and J. J. Grabowski, *Chem. Rev.* 92, 1611 (1992).

<sup>21</sup>Vural S, Seekin T., "Brush-type surface modification of Kapton with a new approach", *Adv Polym Technol.* 2018;37:1703-1711. <https://doi.org/10.1002/adv.21827>

<sup>22</sup>Ftir and dielectric studies of electrical aging in polyimide under AC voltage. (2012). *IEEE Transactions on Dielectrics and Electrical Insulation, Dielectrics and Electrical Insulation, IEEE Transactions on, IEEE Trans. Dielect. Electr. Insul*, (2), 574. <https://doi-org.libproxy.unm.edu/10.1109/TDEI.2012.6180252>

<sup>23</sup>Inagaki, N., Tasaka, S., & Masumoto, M. (1996). Improved Adhesion between Kapton Film and Copper Metal by Plasma Graft Polymerization of Vinylimidazole. *MACROMOLECULES*, (5), 1642. All rights reserved: BRITISH LIBRARY BOARD

<sup>24</sup>Konno, H., Shiba, K., Kaburagi, Y., Hishiyama, Y., & Inagaki, M. (2001). Carbonization and graphitization of Kapton-type polyimide film having boron-bearing functional groups.

CARBON -AMERICAN CARBON COMMITTEE-, (11), 1731. All rights reserved:  
BRITISH LIBRARY BOARD

<sup>25</sup>Hegazy, E.-S. A., Sasuga, T., Nishii, M., & Seguchi, T. (1992). Irradiation effects on aromatic polymers: 2. Gas evolution during electron-beam irradiation. *Polymer*, 33(14), 2904–2910. [https://doi-org.libproxy.unm.edu/10.1016/0032-3861\(92\)90075-8](https://doi-org.libproxy.unm.edu/10.1016/0032-3861(92)90075-8)

<sup>26</sup>Trautmann, C., Schwartz, K., & Steckenreiter, T. (1999). Specificity of ion induced damage. *NUCLEAR INSTRUMENTS AND METHODS IN PHYSICS RESEARCH SECTION B*, (1–4), 162. Retrieved from <https://search-ebsohost-com.libproxy.unm.edu/login.aspx?direct=true&db=edsbl&AN=RN069912758&site=eds-live&scope=site>

<sup>27</sup>van Duin, A. C. T., Dasgupta, S., Lorant, F., & Goddard, W. A. (2001). ReaxFF: A Reactive Force Field for Hydrocarbons. *JOURNAL OF PHYSICAL CHEMISTRY A*, (41), 9396. Retrieved from <https://searchebsohostcom.libproxy.unm.edu/login.aspx?direct=true&db=edsbl&AN=RN103411087&site=eds-live&scope=site>

<sup>28</sup>Rahnamoun, A., Engelhart, D. P., Humagain, S., Koerner, H., Plis, E., Kennedy, W. J., ... van Duin, A. C. T. (2019). Chemical dynamics characteristics of Kapton polyimide damaged by electron beam irradiation. *Polymer*, 176, 135 – 145. <https://doi-org.libproxy.unm.edu/10.1016/j.polymer.2019.05.035>

<sup>29</sup>R. Cooper, R. Hoffmann, (2015), Technical Report, “Jumbo Space Environment Simulation and Spacecraft Charging Chamber Characterization”

<sup>30</sup>“Conductivity Theory and Practice”, D61M002 • Printed by Radiometer Analytical SAS • France • 2004-05B All rights reserved  
[http://www.analyticalchemistry.uoc.gr/files/items/6/618/agwgimometria\\_2.pdf](http://www.analyticalchemistry.uoc.gr/files/items/6/618/agwgimometria_2.pdf)

<sup>31</sup>“Home/Resistors/Resistivity”, <https://www.electronics-tutorials.ws/resistor/resistivity.html>

<sup>32</sup>Frederickson, A.R. and J. Dennison, Measurement of conductivity and charge storage in insulators related to spacecraft charging. IEEE Transactions on Nuclear Science, 2003. 50(6): p. 2284-2291.

<sup>33</sup>Z. Song, C. Ong, H. Gong. “Secondary and backscattered electron yields of polymer surface under electron beam irradiation”. Appl. Surf. Sci. vol. 119, no. 1, pp. 169-75, Sept. 1997. DOI. 10.1016/S0169-4332(97)00182-7.

<sup>34</sup>J.R. Taylor, *An Introduction to Error Analysis: The Study of Uncertainties in Physical Measurements*. University Science Books, 1982.

<sup>35</sup>“History of Spectroscopy”, <http://www.quimica3d.com/ir/en/introduction.php>

<sup>36</sup>Larkin, P. (2011). Infrared and raman spectroscopy. [electronic resource] : principles and spectral interpretation. Elsevier. Retrieved from <https://search-ebSCOhost-com.libproxy.unm.edu/login.aspx?direct=true&db=cat06111a&AN=unm.EBC692432&site=eds-live&scope=site>

<sup>37</sup>S.Yerli, S. Sunatepe, G. Çalışkan, “History of IR and FT-IR”, <https://studylib.net/doc/9612011/history-of-ir-and-ft-ir>

<sup>38</sup>Module 2: Spectroscopy Techniques, Lecture 10: Infrared Spectroscopy, “Infrared Spectroscopy” <https://nptel.ac.in/courses/102103044/module2/lec10/1.html>

<sup>39</sup>A. Winter, “How to find functional groups in the IR spectrum” <https://www.dummies.com/education/science/chemistry/how-to-find-functional-groups-in-the-ir-spectrum/>

<sup>40</sup>Phenyl Group, “Illustrated Glossary of Organic Chemistry”,  
[http://www.chem.ucla.edu/~harding/IGOC/P/phenyl\\_group.html](http://www.chem.ucla.edu/~harding/IGOC/P/phenyl_group.html)

<sup>41</sup>“Kapton”, <https://en.wikipedia.org/wiki/Kapton>

<sup>42</sup>Rahnamoun, A., Engelhart, D. P., Humagain, S., Koerner, H., Plis, E., Kennedy, W. J., ... van Duin, A. C. T. (2019). Chemical dynamics characteristics of Kapton polyimide damaged by electron beam irradiation. *Polymer*, 176, 135–145. <https://doi-org.libproxy.unm.edu/10.1016/j.polymer.2019.05.035>

<sup>43</sup>N. Birkner, Q. Wang, (2019), “How an FTIR Spectrometer Operates”  
[https://chem.libretexts.org/Bookshelves/Physical\\_and\\_Theoretical\\_Chemistry\\_Textbook\\_Maps/Supplemental\\_Modules\\_\(Physical\\_and\\_Theoretical\\_Chemistry\)/Spectroscopy/Vibrational\\_Spectroscopy/Infrared\\_Spectroscopy/How\\_an\\_FTIR\\_Spectrometer\\_Operates](https://chem.libretexts.org/Bookshelves/Physical_and_Theoretical_Chemistry_Textbook_Maps/Supplemental_Modules_(Physical_and_Theoretical_Chemistry)/Spectroscopy/Vibrational_Spectroscopy/Infrared_Spectroscopy/How_an_FTIR_Spectrometer_Operates)

<sup>44</sup>Nurmukhametov, R.; Likhachev, D.Y.; Lavrov, S.; Kardash, J.Y. Features of electronic absorption spectra of aromatic polyimides and polyisoimides. *Polym. Sci. USSR* **1989**, 31, 434–440, doi:10.1016/0032-395090402-4.

<sup>45</sup>Atta, A. Modification of the Surface Properties of Polyimide Films Using Oxygen Plasma Exposure. *Arab J. Nucl. Sci. Appl.* **2013**, 46, 115–123.

<sup>46</sup>School of Materials Science and Engineering, UNSW Sydney, “Stress and Strain,”  
<http://www.materials.unsw.edu.au/tutorials/online-tutorials/stress-and-strain-0>

<sup>47</sup>A. Peshin, “What Is The Stress-Strain Curve?”  
<https://www.scienceabc.com/innovation/what-is-the-stress-strain-curve.html>

<sup>48</sup>TA Universal Instruments, “DMA Q800 Specifications”,  
<http://www.tainstruments.com/wp-content/uploads/dma.pdf>

<sup>49</sup>Smith, A.L., *The Coblenz Society Desk Book of Infrared Spectra* in Carver, C.D., editor, *The Coblenz Society Desk Book of Infrared Spectra, Second Edition*, The Coblenz Society:Kirkwood, MO, 1982, pp 1-24. A [PDF file](#) of this article is available (reproduced with permission of the Coblenz Society).

<sup>50</sup>Coblenz Society, Inc., "Evaluated Infrared Reference Spectra" in **NIST Chemistry WebBook, NIST Standard Reference Database Number 69**, Eds. P.J. Linstrom and W.G. Mallard, National Institute of Standards and Technology, Gaithersburg MD, 20899, <https://doi.org/10.18434/T4D303>, (retrieved June 6, 2019).

<sup>51</sup>Min, J.; Tao, Z.; Song, X.; Zhang, J.; Wang, Z.; Ji, Y.; Zhai, G.; Ye, X. Study on electron beam cross-linked ethylene-tetrafluoroethylene copolymer-insulated cables for aerospace applications: Mechanical performance, crystallization kinetics, and fluoride precipitation. *Polym. Adv. Tech.* 2018, 29, 1497–1506, doi:10.1002/pat.4261

<sup>52</sup>Yang, S.L.; Wu, Z.H.; Yang, W.; Yang, M.B. Thermal and mechanical properties of chemical crosslinked polylactide (PLA). *Polym. Test.* 2008, 27, 957–963, doi:10.1016/j.polymertesting.2008.08.009

<sup>53</sup>Hou, L.; Wu, Y.; Guo, B.; Shan, D.; Zong, Y. Degeneration and damage mechanism of epoxy-based shape memory polymer under 1 MeV electron irradiation. *Mater. Lett.* 2018, 222, 37–40, doi:10.1016/j.matlet.2018.03.186